Macrofracturing of Oceanic Lithosphere in Complex Large Earthquake Sequences

Thorne Lay[1] [iD], **Lingling Ye[2]** [iD], **Zhenbo Wu[1,3]** [iD], **and Hiroo Kanamori[4]** [iD]

[1]Earth and Planetary Sciences Department, University of California, Santa Cruz, CA, USA, [2]Guangdong Provincial Key Lab of Geodynamics and Geohazards, School of Earth Sciences and Engineering, Sun Yat-sen University, Guangzhou, China, [3]College of Geophysics, Chengdu University of Technology, Chengdu, China, [4]Seismological Laboratory, California Institute of Technology, Pasadena, CA, USA
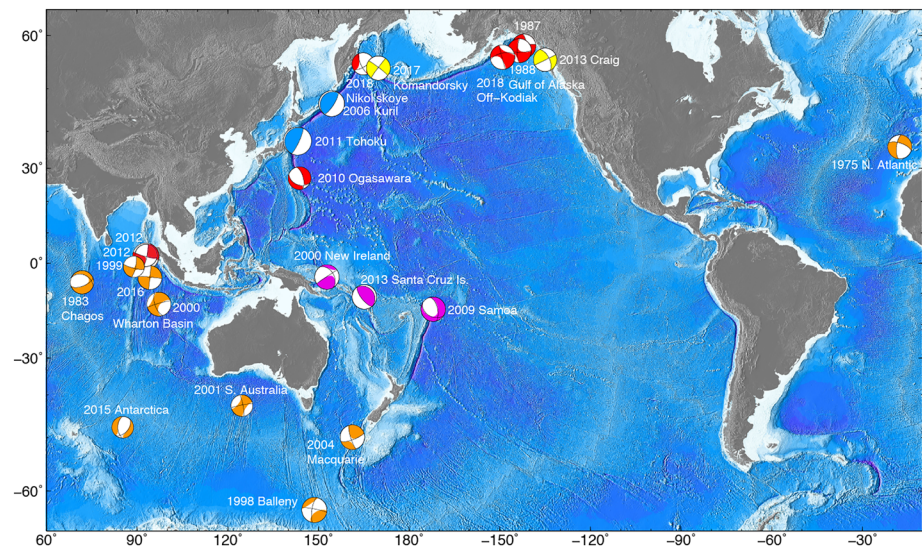
Abstract Major earthquakes in oceanic lithosphere seaward of the subduction zone outer trench slope are relatively uncommon, but several recent occurrences have involved very complex sequences rupturing multiple nonaligned faults and/or having high aftershock productivity with diffuse distribution. This includes the 21 December 2010 M_W 7.4 Ogasawara (Bonin), 11 April 2012 M_W 8.6 Indo-Australia, 23 January 2018 M_W 7.9 Off-Kodiak Island, and 20 December 2018 M_W 7.3 Nikol'skoye (northwest Pacific) earthquakes. Major oceanic intraplate event sequences farther from plate boundaries do not tend to be as complex in faulting or aftershocks. Outer trench slope extensional faulting can involve complex distributed sequences, particularly when activated by great megathrust ruptures such as 11 March 2011 M_W 9.1 Tohoku and 15 November 2006 M_W 8.3 Kuril Islands. Intense faulting sequences also occur near subduction zone corners, with many fault geometries being activated, including some in nearby oceanic lithosphere, as for the 29 September 2009 M_W 8.1 Samoa, 6 February 2013 M_W 8.0 Santa Cruz Islands, and 16 November 2000 M_W 8.0 New Ireland earthquakes. The laterally varying plate boundary stresses from heterogeneous locking, recent earthquakes, or boundary geometry influence the specific faulting geometries activated in nearby major intraplate ruptures in oceanic lithosphere. Preexisting lithospheric structures and fabrics exert secondary influences on the faulting. Intraplate stress release in oceanic lithosphere near subduction zones favors distributed macrofracturing of near-critical fault systems rather than localized, single-fault failures, both under transient loading induced by plate boundary ruptures and under slow loading by tectonic motions and slab pull.

1. Introduction

Most of Earth's largest earthquakes are associated with convergent plate tectonic boundaries, predominantly involving interplate thrust faulting that directly accommodates plate convergence. However, large intraplate faulting within the oceanic lithosphere prior to subduction also plays important roles, with deformation driven by a superposition of slab-pull bending stresses and cycling plate boundary frictional stresses. Many studies of oceanic intraplate earthquakes have focused on the outer trench slope environment that primarily involves shallow normal faulting with tension axes nearly orthogonal to the trench (e.g., Christensen & Ruff, 1988; Craig et al., 2014; Sladen & Trevisan, 2018). Following great interplate thrust events, very complex extensional faulting sequences can occur in the outer trench slope region and outer rise, especially if the interplate thrust faulting extends to near the trench (e.g., Sladen & Trevisan, 2018; Wetzler et al., 2017). The fracturing of subducting oceanic lithosphere abets water penetration into the plate, impacting arc magmatism and seismogenic behavior of subducted slabs (e.g., Boneh et al., 2019; Faccenda et al., 2009; Ranero et al., 2003).

There are relatively few large oceanic intraplate earthquakes seaward of the outer rise (e.g., Lay, 2019), but recent examples of such events have involved remarkably complex distributed faulting. Each such sequence has unique local conditions, plate stresses, and tectonic fabrics in the plate, and it is often difficult to account for the specific complexity of the faulting. Here we consider the collective observations of major complex intraplate event sequences in oceanic lithosphere as it approaches subduction zones to work toward a better understanding of why relatively old, stiff oceanic lithosphere fractures in this manner. We consider all intraplate events seaward of the outer trench slope activity in major subduction zones with $M_W \geq 7.0$ from 1975 to 2019, along with several examples of near-plate boundary sequences for comparison. The USGS-National

Figure 1. Major and great earthquake Global Centroid Moment Tensor (GCMT) solutions for all intraplate ruptures in oceanic lithosphere seaward of the subduction zone outer trench slope with multifault ruptures and/or extensive aftershock sequences from 1975 to 2019 with $M_W \geq 7.0$ (red focal mechanisms), all intraplate oceanic ruptures far from trenches from 1975 to 2019 with $M_W \geq 7.0$ (orange focal mechanisms), two example great interplate ruptures that activate extensive outer trench slope and outer rise sequences (blue focal mechanisms), two example strike-slip events on plate boundaries far from ridges (yellow focal mechanisms), and three example events near corners in subduction zones with multifault sequences that include intraplate and interplate ruptures (purple focal mechanisms).

Earthquake Information Center (NEIC) catalog does not list any additional major intraplate oceanic events well seaward of the outer trench slope back to 1956 and only lists about 10 such events from 1900 to 1955. Lacking details about those events and their aftershocks, we do not consider them here.

Various major oceanic earthquake sequences from 1975 to 2019 considered here are indicated in Figure 1 by the Global Centroid Moment Tensor solution (https://www.globalcmt.org/CMTsearch.html) or independently determined mechanism (for 1975 North Atlantic) for the largest event in each sequence. Table 1 lists event details from the USGS-NEIC (https://earthquake.usgs.gov/earthquakes/search/), and Table 2 summarizes key attributes of each of the oceanic faulting sequences considered, noting principal features of each environment. The compressional quadrants are colored by sequence type. Red mechanisms indicate large intraplate events just seaward of the subduction zone outer rise that involve particularly complex faulting, such as 1987 M_W 7.9 and 1988 M_W 7.8 Gulf of Alaska, 2010 M_W 7.3 Ogasawara, 2012 M_W 7.2 Wharton Basin, 2012 M_W 8.6 Indo-Australia, 2018 M_W 7.9 Off-Kodiak Islands, and 2018 M_W 7.3 Nikol'skoye. Orange mechanisms indicate large intraplate events relatively far from subduction zones, such as 1975 M_W 7.9 North Atlantic, 1983 M_W 7.3 Chagos, 1998 M_W 8.1 Balleny Islands, 2001 M_W 7.1 South of Australia, 1999 M_W 7.0, 2000 M_W 7.9 and 2016 M_W 7.8 Wharton Basin, 2004 M_W 8.1 Macquarie, and 2015 M_W 7.1 Antarctica. These two categories are our primary focus, with the events shown representing all such events found in the NEIC catalog with $M_W \geq 7.0$ from 1975 (actually extending back through 1956) to 2019. We will focus on the events with $M_W \geq 7.3$, as resolution of faulting and aftershock distribution complexity is low for smaller events.

Some additional oceanic sequences indicated in Figure 1 are considered to illustrate temporal and spatial stress variation influences on the intraplate faulting. Blue mechanisms indicate examples of great interplate thrust events that activate particularly extensive oceanic outer trench slope to outer rise aftershock sequences, such as 2006 M_W 8.4 Kuril Islands and 2011 M_W 9.1 Tohoku. Purple mechanisms indicate examples of complex sequences involving a mix of interplate and intraplate faulting near corners in subduction zones where oceanic lithosphere may be strongly contorted and intraplate stress is complex, such as 2000 M_W 8.0 New Ireland, 2009 M_W 8.1 Samoa, and 2013 M_W 8.0 Santa Cruz Islands. Yellow mechanisms are examples of strike-slip events on oceanic plate boundaries far from ridges, such as 2013 M_W 7.5 Craig and 2018 M_W 7.3 Komadorsky (Bering Island).

Table 1
Mainshocks of Diverse Sequences Involving Fracture of Oceanic Lithosphere (USGS-NEIC Parameter), With Observed Na (obs)[4.5, M-3.0] and Predicted Na (pred) [4.5] Aftershock Productivity

Sequence mainshock	UTC	Lat./Lon.	M_W	Na (obs)	Na (pred)
Major Intraplate Oceanic Earthquakes Just Seaward of Subduction Zone Outer Rise					
17 Nov. 1987 Gulf of Alaska(1)	08:46:53	58.6°N,143.3°W	7.1	7[a], 9[b]	16
30 Nov. 1987 Gulf of Alaska(2)	19:23:19	58.7°N, 142.8°W	7.9	21, 10	98
6 Mar. 1988 Gulf of Alaska(3)	22:35:38	57.0°N, 143.0°W	7.8	12, 8	78
21 Dec. 2010 Ogasawara/Bonin	17:19:40	26.9°N, 143.7°E	7.4	471, 592[b]	31
10 Jan. 2012 Wharton Basin	18:36:59	2.4°N, 93.2°E	7.2	21, 23[b]	20
11 Apr. 2012 Indo-Australia	08:38:36	2.4°N, 93.1°E	8.6	314, 14	483
23 Jan. 2018 Off-Kodiak Island	09:31:40	56.0°N, 149.2°W	7.9	45, 14	98
20 Dec. 2018 Nikol'skoye	17:01:55	55.1°N, 164.7°E	7.3	62, 98[b]	25
Oceanic Intraplate Sequences Away From Spreading Ridges and Trenches					
26 May 1975 N. Atlantic	09:11:51	36.0°N, 17.6°W	7.9	10, 2	98
30 Nov. 1983 Chagos	17:46:00	6.9°S, 72.1°E	7.3	75, 79[b]	25
25 Mar. 1998 Balleny Islands	03:12:25	62.9°S, 149.5°E	8.1	24, 7	154
15 Nov. 1999 Indian Plate	05:42:43	1.3°S, 89°E	7.0	6, 7[b]	13
18 June 2000 Wharton Basin	14:44:13	13.8°S, 97.5°E	7.9	11, 6	98
12 Dec. 2001 S. of Australia	14:02:35	42.8°S, 124.7°E	7.1	7, 12[b]	16
23 Dec. 2004 Macquarie	14:59:04	49.3°S, 161.3°E	8.1	26, 4	154
4 Dec. 2015 Antarctica	22:25:00	47.6°S, 85.1°E	7.1	3, 3[b]	16
2 Mar. 2016 Wharton Basin	12:49:48	5.0°S, 94.3°E	7.8	14, 5	78
Example Great Interplate Thrust Events Producing Oceanic Outer Trench Slope Sequences					
15 Nov. 2006 Kuril	11:14:13	46.6°N, 153.3°E	8.3	652, 57	244
11 Mar. 2011 Tohoku, Japan	05:46:24	38.3°N, 142.4°E	9.1	2,298, 49	1,510
Example Great Oceanic Sequences Near Subduction Zone Corners					
16 Nov. 2000 New Ireland	04:54:56	4.0°S, 152.2°E	8.0	462, 182	123
29 Sept. 2009 Samoa	17:48:10	15.5°S, 172.1°W	8.1	285, 79	154
6 Feb. 2013 Santa Cruz Island	01:12:25	10.8°S, 165.1°E	8.0	536, 189	123
Example Oceanic Interplate Strike-Slip Sequences Away from Spreading Ridges					
5 Jan. 2013 Craig, Alaska	08:58:14	55.2°N, 134.9°W	7.5	10, 10	39
17 Jul. 2017 Komandorsky Is.	23:34:13	54.4°N, 168.9°E	7.7	47, 25	62

[a]Time window truncated by M_W 7.9 on 30 November 1987. $M_S = 6.9$ given by NEIC, M_W 7.1 from GCMT.   [b]Lower bound estimate as M_W~3 is less than 4.5 completeness level.

As shown below, earthquake sequences in relatively old oceanic lithosphere just seaward of the outer trench slope in subduction zones (red mechanisms in Figure 1) tend to be notably complex in terms of involving rupture of multiple fault planes with distinct orientations during the mainshocks and/or having very productive widely distributed aftershock activity off the main fault. Intraplate faulting farther from plate boundaries tends to involve less faulting and aftershock diversity. Given their diversity and distinct locations, the trend of greater sequence complexity for intraplate events just seaward of the trench slope is not straightforward to account for. In this study, we systematically compare the mainshock rupture behavior and aftershock productivity of major event sequences in oceanic settings to shed light on possible mechanisms controlling the faulting and seismicity complexity.

2. Major Intraplate Sequences Within Oceanic Lithosphere

Given that the rupture sequences of most of the events shown in Figure 1 and listed in Table 1 have been extensively studied by various investigators, we first provide quantification of the less-studied mainshocks; the 2010 Ogasawara and 2018 Nikol'skoye events. Short- and intermediate-period *P* wave recordings from networks of stations at different azimuths are used in back projections (Xu et al., 2009) to determine space-time distributions of coherent bursts of short period energy that constrain the overall rupture expansion characteristics. Kinematic space-time slip distributions with variable subfault rake and flexibly parameterized subfault source time functions are determined by least squares inversions (e.g., Hartzell & Heaton, 1983; Kikuchi & Kanamori, 1991; Ye et al., 2016) of large data sets of broadband *P* and *SH* waves. These solutions supplement preliminary solutions obtained by the USGS-NEIC.

Table 2
Tectonic Features of Each Source Region

Event	Lateral variation of plate coupling	Geometrical complexity of plate boundary (e.g., corner)	Major bathymetric features	Great earthquake trigger	Large distance from plate boundary, ridge, or fracture zone
1975 North Atlantic					X
1983 Chagos					X
1987 Gulf of Alaska	X			1964 Alaska?	
1988 Gulf of Alaska	X			1964 Alaska?	
1998 Balleny Is.					X
1999 Indian Plate					X
2000 Wharton Basin					X
2000 New Ireland		X			
2001 South of Australia					X
2004 Macquarie					Near Transform
2006 Kuril				X	
2009 Samoa		X			
2010 Ogasawara	X		X		
2011 Tohoku				X	
2012 Wharton Basin	X			2004 Sumatra?	
2012 Indo-Australia	X			2004 Sumatra?	
2013 Craig					Transform Fault
2013 Santa Cruz Is.		X			
2015 Antarctica					Off Ridge
2016 Wharton Basin					X
2017 Komandorsky					Sliver Fault
2018 Off-Kodiak	X			1964 Alaska?	
2018 Nikol'skoye	X	X	X		

2.1. The 2010 Ogasawara Sequence

The 21 December 2010 M_W 7.4 Ogasawara event (Table 1) has a remarkably productive aftershock sequence, as discussed by Obana et al. (2014). The sequence occurred on the northern end of a region where the Bonin Trench is significantly narrowed and shallowed over an ~100 km length by influx of the buoyant Ogasawara Plateau which has significant bathymetric relief (Figure 2). The Pacific and Philippine Sea plates are converging in this region at a rate of about 40 mm/year. The 2010 sequence is generally situated relative to the arc at a distance where outer trench slope activity occurs along the deep trench to the north, but the 2010 activity extends more than 140 km obliquely seaward from the contact with the Philippine Sea plate. The overall trend of the activity is parallel to a fracture zone in the seafloor across which the plate age varies from ~135 to 145 Ma (Obana et al., 2014), but it is not tightly aligned on the trace of the fracture zone.

Overall, the rupture process of the 2010 Ogasawara mainshock appears to be rather simple, and the preferred slip model with strike 113° and dip 46° is compared with aftershock seismicity in Figure 2. Details about the long-period point-source inversions, back projections (Figure S1 in the supporting information), and finite-source inversions for this event (Figures S2–S6) are given in supporting information Text S1. The primary region of concentrated slip is moderately depleted in aftershock activity, but based on the shallow depth extent of the mainshock and the diffuse distribution of aftershock locations and focal mechanisms, it appears that multiple faults must have activated during the sequence, with those to the northwest having strike rotated closer to trench-parallel, along the trend of the fracture zone. Obana et al. (2014) find that the aftershocks form three subparallel lineations along the fracture zone and that they outline the mainshock rupture area over an ~80 km long stretch during the first hour and then migrate northwestward, southeastward, and eastward from the mainshock region. Note that the dip of the mainshock cannot account for the widespread aftershock distribution by near-mainshock-fault events. The fault plane used in Figures 2 and S2, similar to that preferred by the USGS-NEIC, does not correspond to the fracture zone trend, suggesting that the rupture may be more influenced by the lateral structure of the Ogasawara Plateau and slab pull stresses from the subducted Bonin slab toward the west.
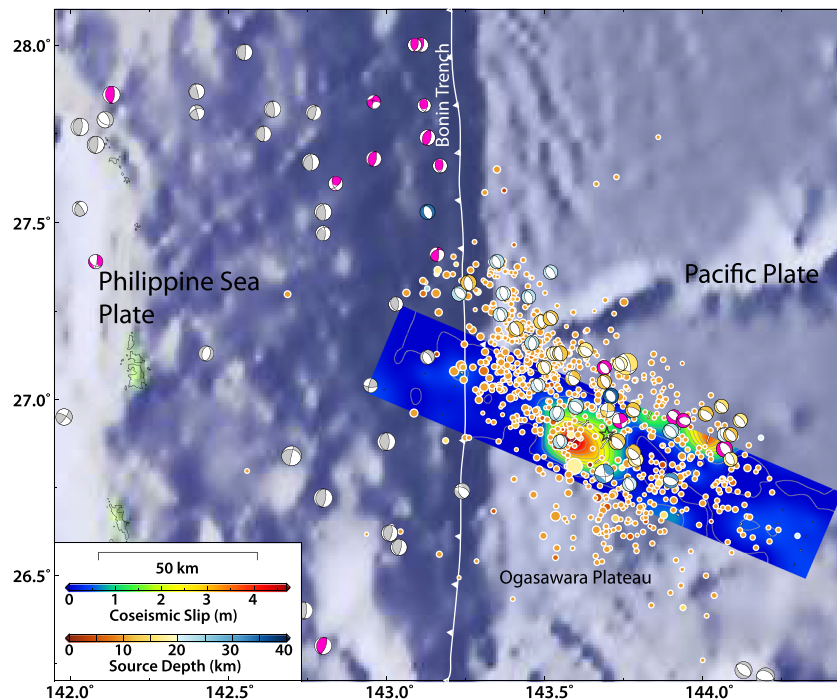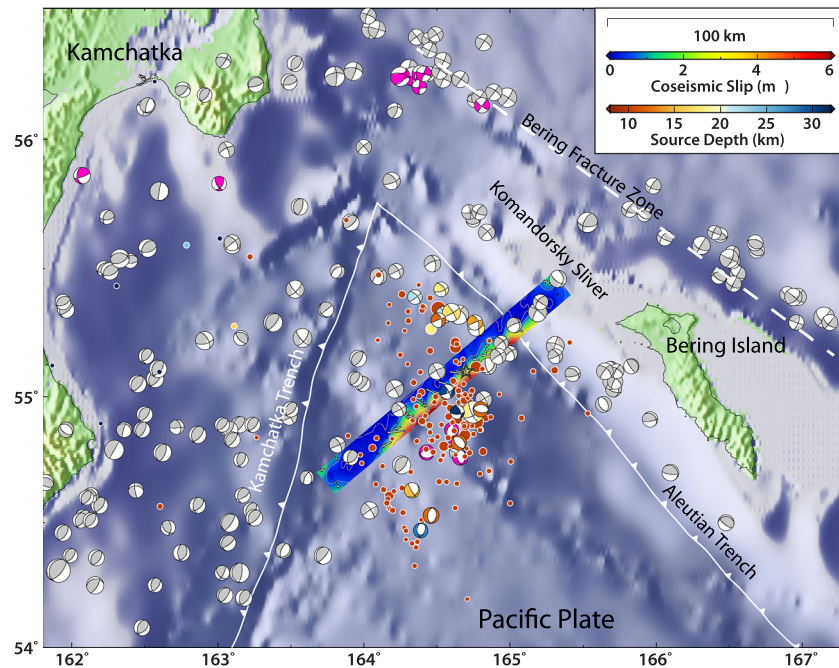
Figure 2. Map showing the 2010 Ogasawara M_W 7.4 mainshock finite-slip model from Figure S2 (the star indicates the mainshock epicenter) along with aftershocks in the first 60 days after the event from the USGS-NEIC catalog (circles colored by source depth and with radius proportional to magnitude) and GCMT focal mechanisms plotted at the centroid locations, colored by centroid depth and scaled by M_W. Focal mechanisms colored in gray and magenta are for the time periods of 1976 to 2010 before the mainshock and 2011 to 2019 after the mainshock, respectively. The background bathymetry indicates the position of the Bonin trench trending north-south near longitude 143.2°, approximated by the white saw-toothed curve.

2.2. The 2018 Nikol'skoye Sequence

The 20 December 2018 Nikol'skoye (Bering Island) M_W 7.3 event (Table 1) has a highly productive aftershock sequence, with spatially distributed strike-slip and oblique normal faulting mechanisms (Figure 3). The sequence extends to about 100 km from the subduction zone along Kamchatka and lies just southwest of the Aleutian subduction zone, where almost no convergence occurs along this stretch of the arc. Instead, the Komandorsky sliver is translating parallel to the Aleutian trench at a high percentage (~65%) of the plate motion velocity between the Pacific and the Bering Plate (e.g., Kogan et al., 2017; Lay et al., 2017). The northwestern edge of the sliver collides with Kamchatka adjacent to the subduction zone along which the Pacific plate subducts beneath the peninsula. The seafloor near the 2017 sequence has significant variation in topography and lies along the Emperor Island chain just to the south, as it impinges on the Kamchatka subduction zone (Figure 1) with hot-spot volcanism dated to >81 Ma (e.g., Portnyagin et al., 2008).

Combining information from various seismic observations, our preferred slip model for the 2018 Nikol'skoye event has a fault plane with strike 230° and dip 66° (Figure 3). Details about the long-period point-source inversions, back projections (Figure S7), and our finite-fault slip inversions (Figures S8–S12) for this event are given in supporting information Text S2. For the rupture model in Figure 3, the tension axis and fault plane are highly oblique to the Kamchatka subduction zone. The area of large slip in the model traverses the aftershock distribution, but there is no clear localization of aftershocks onto the fault plane, even allowing for the nonvertical dip of the mainshock plane. The alternate choice of fault plane (Figure S10), preferred by the USGS-NEIC, also shows large deviation from the aftershock pattern (Figure S12). The overall sequence involves oblique deformation of the old Pacific lithosphere seaward of the trench, with complex activation of multiple faults.

Figure 3. Map showing the 2018 Nikol'skloye M_W 7.4 mainshock finite-slip model from Figure S8 along with aftershocks in the first 60 days after the event from the USGS-NEIC catalog (circles with radius proportional to magnitude) and GCMT focal mechanisms plotted at the centroid locations, colored by centroid depth, and scaled by M_W. Focal mechanisms colored in gray and magenta are for the time periods of 1976 to 2018 before the mainshock and 2018 to 2019 after the mainshock, respectively. The Aleutian Trench has no convergence in this region, with the Komandorsky Sliver moving parallel to the Pacific plate motion with right-lateral shearing on the Bering Fracture Zone.

2.3. Relative Aftershock Productivity

Now we proceed to discuss the general faulting and seismicity patterns of the various earthquake sequences indicated in Figure 1. For each sequence with a mainshock $M_W \geq 7.3$, a map will be shown along with a time line, including all aftershocks within 60 days of the mainshock reported in the USGS-NEIC catalog, along with all Global Centroid Moment Tensor (GCMT) focal mechanisms for events in the 60 day sequence. The search area for aftershocks was specified by a circle with radius R (in km) equal to twice the empirical rupture length from Wells and Coppersmith (1994), that is, $R = 2 \times 10^{-2.44 + 0.59 Mw}$, using M_W from the GCMT catalog. We constrain aftershock depths to be within ±30 km of the mainshock depth. The specific search parameters are not critical for this study, but the count of aftershocks with magnitudes ≥ 4.5 (4.5 is an optimistic estimate of completeness level for the USGS-NEIC catalog adopted from Dascher-Cousineau et al. [2020]), in the 60 day window allows us to compare productivity of each sequence in a consistent manner. Using the same space-time windowing for all 570 global shallow mainshocks with $M_W \geq 7.0$ from 1976 to 2019 results in a reference aftershock productivity curve given by $Na = 10^{0.99 Mw - 5.83}$, where Na is the number of aftershocks with magnitude ≥ 4.5 (Ye et al., 2020). This is compatible with productivity relations determined for a wider range of mainshock sizes by Dascher-Cousineau et al. (2020). The predicted reference aftershock productivity [Na (pred)], representing the median value for all shallow events of corresponding magnitude, is listed in Table 1 for comparison with the observed number, Na (obs)[4.5], and the ratio Na (obs)/Na (pred) is shown in each time line figure. We also use a fixed three-magnitude unit interval below the mainshock M_W for counting events in the 60 day window, for which a magnitude-dependent scaling correction is not needed. These are the second value Na (obs)[M-3] listed in Table 1. By either measure of productivity, the 2010 Ogasawara and 2017 Nikol'skoye events stand out. By evaluating productivity above the estimated global completeness level, our measures are not sensitive to distance offshore or location of the events. We show all aftershocks recorded by USGS-NEIC for each event but focus on those with $M_W \geq 4.5$, as used for the global productivity calculation.
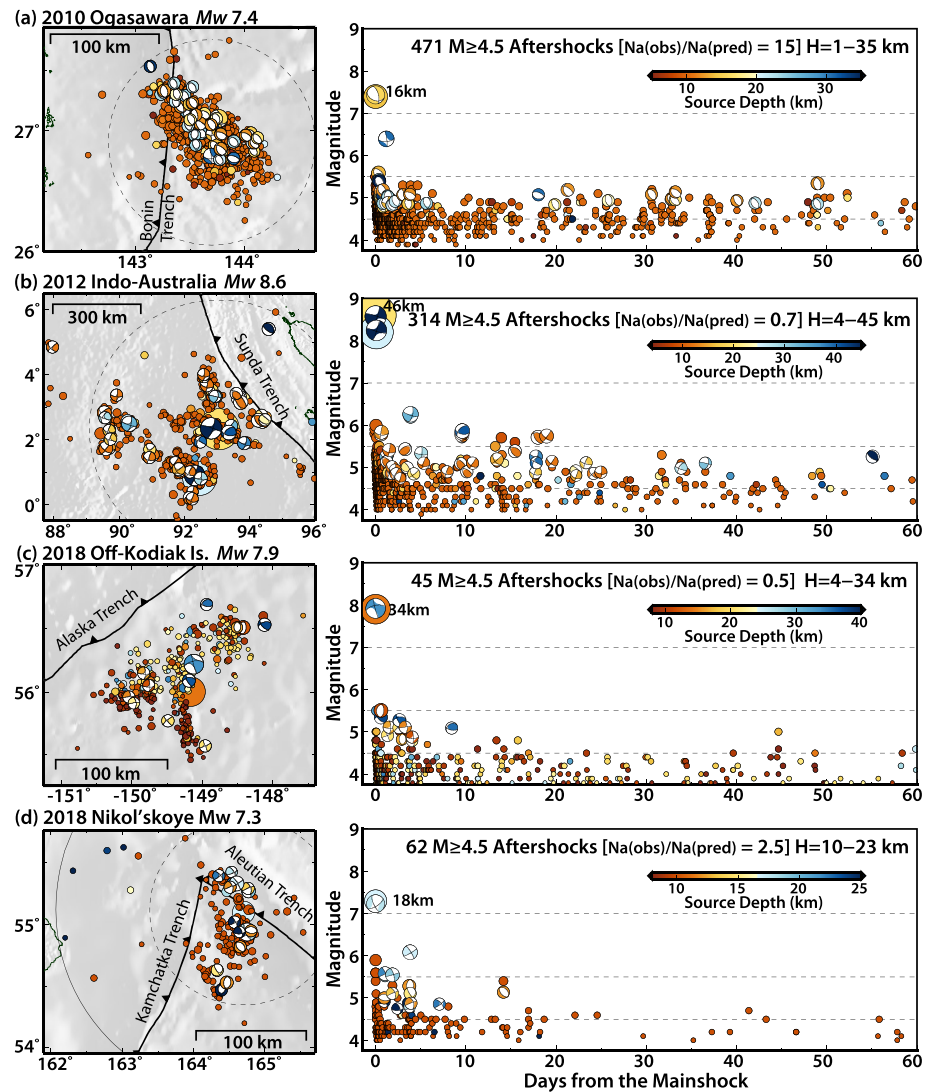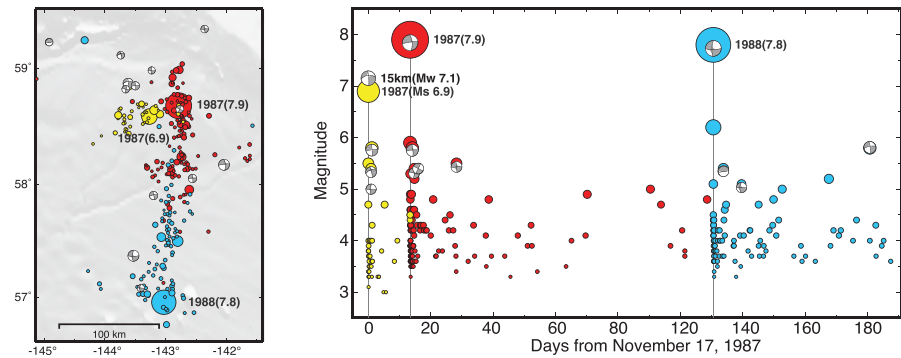
Figure 4. Complex earthquake sequences in oceanic lithosphere seaward of trenches showing 60 day intervals of all seismicity from the USGS-NEIC catalog and all GCMT moment tensor solutions (both colored by source depth and scaled proportional to magnitude) within a two source dimension radius (dashed black lines are one source dimension radii, solid black lines are two source dimensions) from each mainshock for: (a) 2010 Ogasawara (Bonin), (b) 2012 Indo-Australia, (c) 2018 Off-Kodiak Island, and (d) 2018 Nikol'skoye. The number of aftershocks, Na (obs), with $M \geq 4.5$ within the indicated source depth (H) range over the 60 day window is indicated for each event, along with the ratio Na (obs)/Na (pred) from Table 1. The GCMT centroid depth of the mainshock is shown next to the event focal mechanism.

## 2.4. Complex Sequences Seaward of Subduction Zones

The intraplate earthquake sequences in oceanic lithosphere seaward of the outer trench slope highlighted by red focal mechanisms in Figure 1 are displayed in Figures 4 and 5. There is substantial diversity in complexity, which we define as having coseismic rupture on multiple nonaligned faults in the mainshock and/or aftershock sequence, among these major earthquake sequences in relatively old oceanic lithosphere. The event characterizations are all based on remote seismological information, so event size is more of an issue in our characterization of complexity than is location; hence, we focus on the events with $M_W \geq 7.3$.

The 2010 Ogasawara sequence (Obana et al., 2014) involves a remarkably productive sequence for an M_W 7.4 event (Figures 2 and 4a), with 471 aftershocks with magnitude $\geq$ 4.5 in our space-time window, compared to a typical value of 31 (Table 1). Almost all of the known mechanisms involve normal faulting, although a few
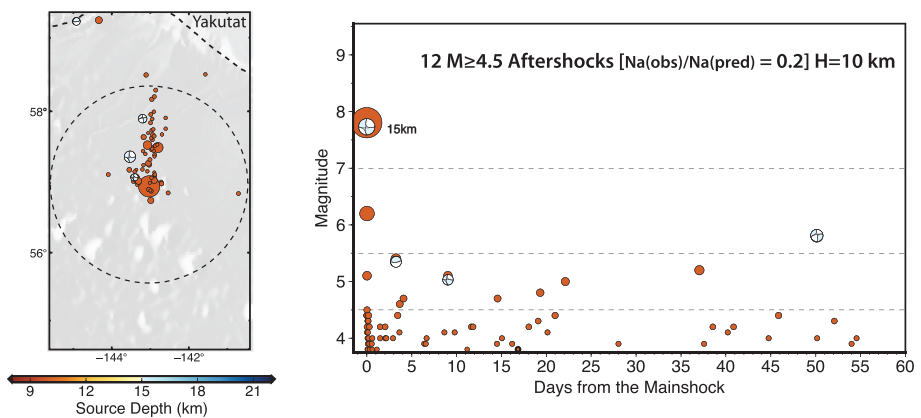
(a) 1987-1988, Gulf of Alaska(1,2,3), *Ms 6.9, Mw 7.9, 7.8*

(b) 1987, Gulf of Alaska(2), *Mw 7.9*
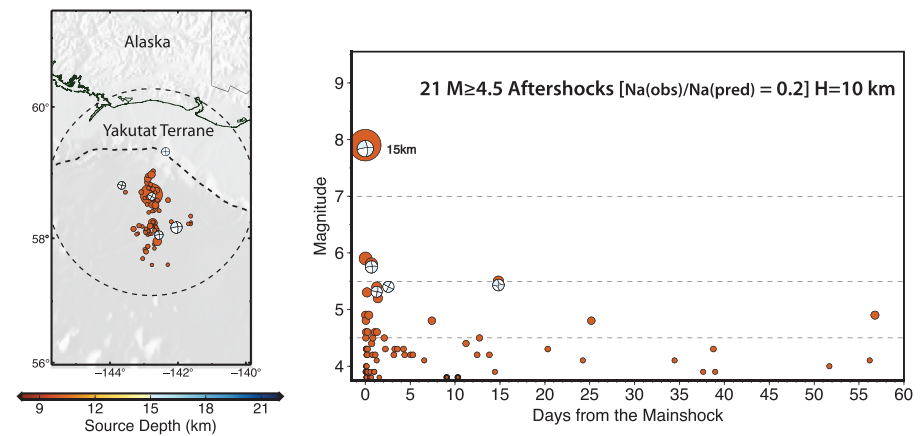
(c) 1988, Gulf of Alaska(3), *Mw 7.8*

Figure 5. (a) Complex earthquake sequence involving a triplet of major events with $M_W = 7.1$, 7.9 and 7.8 initiating 17 November 1987 in ~30 Ma oceanic lithosphere in the Gulf of Alaska in map view (left) and as time series (right) showing a 200 day interval of all seismicity from the USGS-NEIC catalog and all GCMT moment tensor solutions (both colored for each major event and scaled proportional to magnitude). Subsequences (colored by source depth and scaled proportional to magnitude) within a two source dimension radius (dashed black circles are one source dimension radii, and solid black circles are two source dimensions) for the largest mainshocks: (b) 1987 and (c) 1988. The number of aftershocks, *Na* (obs), with $M \geq 4.5$ within the indicated source depth (*H*) range over the 60 day window is indicated for each event, along with the ratio of *Na* (obs)/*Na* (pred) using the reference model discussed in the text. The GCMT centroid depth of the mainshock is shown next to the event focal mechanism.

are highly oblique, with varying strike directions distributed over a broad swath of seismicity about 100 km long by 50 km wide. The sequence trends oblique to the outer rise seaward of the Bonin subduction zone, which has no record of great interplate thrust faulting.

The 2012 Indo-Australian sequence (Figure 4b) involves the largest recorded oceanic strike-slip event with M_W 8.6 and has been extensively studied (e.g., Delescluse et al., 2012; Duputel et al., 2012; Hill et al., 2015; Ishii et al., 2013; Meng et al., 2012; Satriano et al., 2012; Wang et al., 2012; Wei et al., 2013; Wiseman & Bürgmann, 2012; Yadav et al., 2017; Yue et al., 2012; Yue & Lay, 2020; Zhang et al., 2012). With at least four major quasi-orthogonal strike-slip faults rupturing during the mainshock and an M_W 8.2 aftershock on a distinct fault, none of which unambiguously lie along fracture zones in the Wharton Basin and with faulting extending over a region ~500 km wide, this is perhaps the most complex great earthquake sequence yet recorded. Imaging of the sediment-shrouded seafloor in the region indicates the existence of systems of conjugate faults (Singh et al., 2017) in the broad deformation zone extending from the Ninetyeast Ridge to the western Wharton Basin (e.g., Wiens et al., 1985). The M_W 7.2 event in 2012 is moderately productive (Table 1), has a 25 s long rupture duration, and appears to have ruptured the east-west fault, with no clear multiple faulting (Aderhold & Abercrombie, 2016). We do not display that sequence, as it is too compact to characterize well teleseismically.

The 2018 Off-Kodiak Island, Alaska earthquake (Figure 4c) also appears to have ruptured at least four quasi-orthogonal strike-slip faults in the ~30 Ma old Pacific seafloor, seaward of the 1964 Alaska interplate rupture, and has been widely studied as well (e.g., Hossen et al., 2020; Krabbenhoeft et al., 2018; Lay et al., 2018; Ruppert et al., 2018; Wang et al., 2020; Wen et al., 2019; Zhao et al., 2019). The 2012 Indo-Australia and 2018 Off-Kodiak Island events have substantial but not unusual aftershock productivity despite the multiple fault ruptures of the mainshocks (Table 1).

The 2018 Nikol'skoye sequence (Figures 3 and 4d) ruptured in the northwesternmost Pacific plate offshore of the Kamchatka subduction zone, with a very productive earthquake sequence (Table 1) comprised of a widespread mix of normal, thrust and strike-slip faulting.

The other complex oceanic intraplate earthquake sequence indicated in red in Figure 1 involves the 1987–1988 Gulf of Alaska earthquakes (M_W 7.1, 7.9, 7.8) (Figure 5 and Table 1), which are discussed in Lay et al. (2019). While exhibiting less dramatic individual complexity than the sequences in Figure 4, the overall faulting is quite complex, with strike-slip ruptures southwest of the Yakutat Terrane, which is converging with Alaska. The sequence (Figure 5a) began with an M_W 7.1 (M_S 6.9 in the USGS-NEIC catalog) rupture of an east-west trending fault on 17 November 1987 and then ruptured along a north-south trend on 30 November 1987 (M_W 7.9) (Figure 5b) and 6 March 1988 (M_W 7.8) (Figure 5c) (Hwang & Kanamori, 1992; Lahr et al., 1988; Pegler & Das, 1996; Quintanar et al., 1995). The orthogonal faulting sequence resembles a scaled-up version of the 2019 Ridgecrest event.

Only a handful of additional comparable size intraplate earthquakes have been recorded in oceanic lithosphere away from mid-ocean ridges, and these are located further from subduction zones than those in Figure 4. The 1998 Balleny M_W 8.1 earthquake (Figures 1 and 6a) ruptured transverse to well-defined fracture zones in the Antarctic plate seafloor with age of 33–40 Ma along a ~300 km long trend, with multiple aligned fault segments and significant aftershock activity south of the main strike-slip trend (e.g., Antolik et al., 2000; Henry et al., 2000; Hjörleifsdóttir et al., 2009; Kuge et al., 1999; Nettles et al., 1999; Tsuboi et al., 2000).

Three additional major strike-slip earthquakes have ruptured in the Wharton Basin of the Indo-Australian plate at greater distance from the subduction zone than the 2012 sequence (Figure 1). These are the 15 November 1999 (M_W 7.0), 18 June 2000 (M_W 7.9) (Figure 6b), and 2 March 2016 (M_W 7.8) (Figure 6c) earthquakes. These are much less dramatic sequences than those in Figure 4, with relatively compact zones and minor aftershock sequences (Figure 6) that have also been discussed in Lay et al. (2019). The 2000 Wharton Basin mainshock does have some source faulting complexity, indicated by a GCMT solution with a large non-double-couple component (Figures 1 and 6b). The rupture struck west of the Investigator Fracture Zone (Abercrombie et al., 2003; Robinson et al., 2001) and involved two subevents with different mechanisms, with neither clearly located on a fracture zone (Lay, 2019). However, the rupture is much less complex than the comparable size 2018 Off-Kodiak (M_W 7.9) sequence. The 2016 Wharton Basin event has a simple
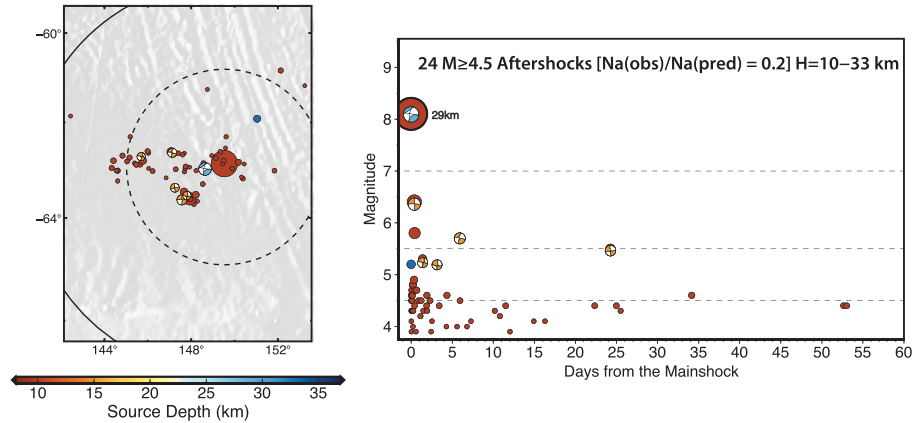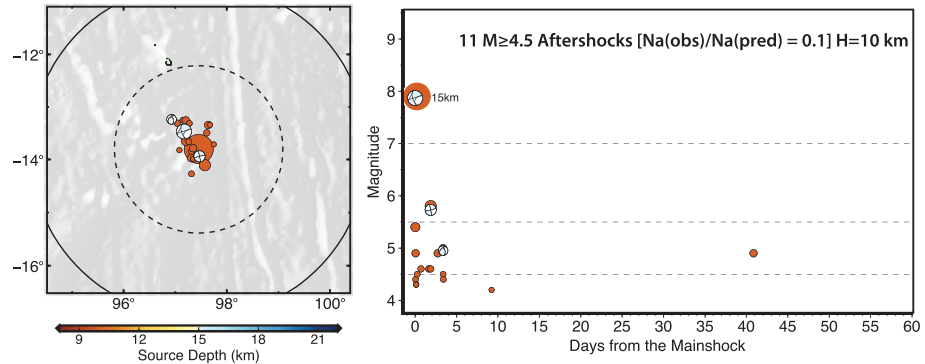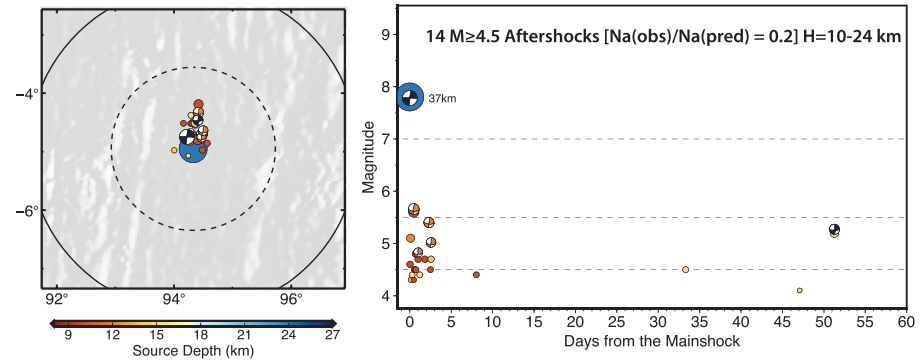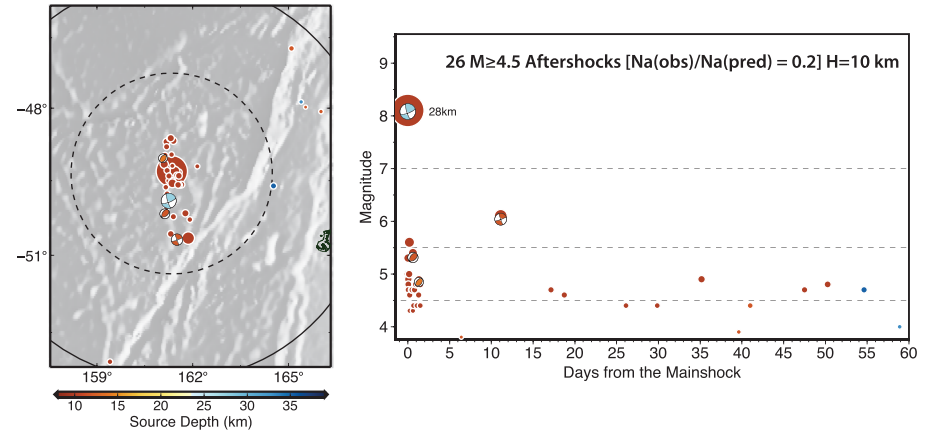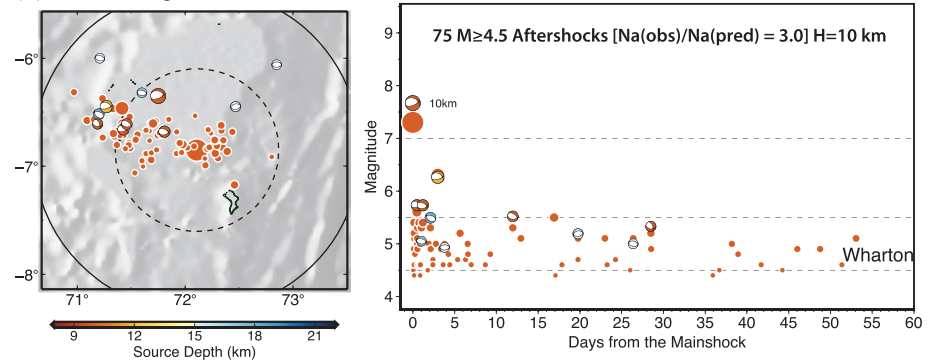
Figure 6. Modest complexity earthquake sequences with mainshock $M_W \geq 7.8$ in oceanic lithosphere well removed from subduction zones in map view and as time series showing 60 day intervals of all seismicity from the USGS-NEIC catalog and all GCMT moment tensor solutions (both colored by source depth and scaled proportional to magnitude) within a two source dimension radius (dashed white lines are one source dimension radii, and solid white lines are two source dimensions) from each sequence mainshock for (a) 1998 Balleny, (b) 2000 Wharton Basin, and (c) 2016 Wharton Basin (Table 1). The latter two events struck within the Indo-Australian plate further away from the subduction zone and outside the intraplate deformation zone where the 2012 sequence occurred. The number of aftershocks, Na (obs), with $M \geq 4.5$ within the indicated source depth (H) range over the 60 day window is indicated for each event, along with the ratio of Na (obs)/Na (pred) using the reference model discussed in the text. The GCMT centroid depth of the mainshock is shown next to the event focal mechanism.

bilateral strike-slip rupture (Gusman et al., 2017; Lay et al., 2016) offset from an adjacent north-south trending fracture zone. The only other major intraplate strike slip events with $M_W \geq 7.3$ on record are the 23 December 2004 Macquarie (M_W 8.1) (Figure 7a) (e.g., Hayes et al., 2009; Kennett et al., 2014; Robinson, 2011), 30 November 1983 Chagos (M_W 7.3) (Figure 7b) (e.g., Wiens & Stein, 1984), and 26 May
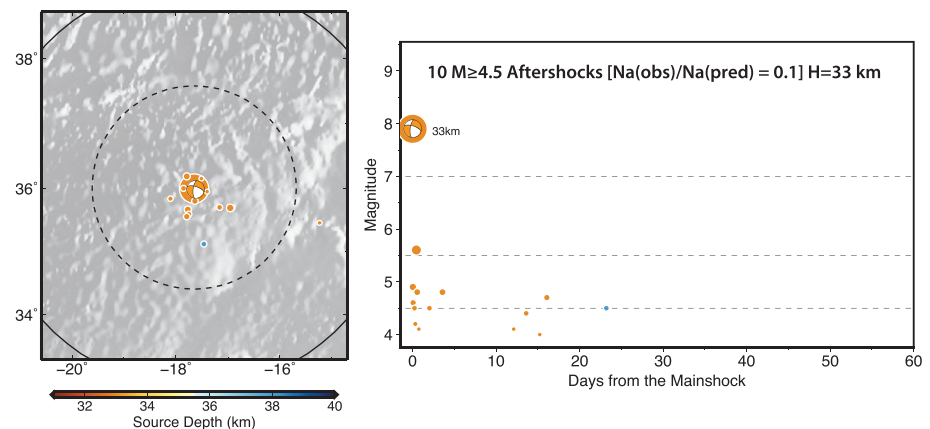
Figure 7. Additional modest complexity earthquake sequences with mainshock $M_W \geq 7.3$ in oceanic lithosphere well removed from subduction zones in map view and as time series showing 60day intervals of all seismicity from the USGS-NEIC catalog and all GCMT moment tensor solutions (both colored by source depth and scaled proportional to magnitude) within a two source dimension radius (dashed white lines are one source dimension radii, and solid white lines are two source dimensions) from each sequence mainshock for (a) 2004 Macquarie; (b) 1983 Chagos, and (c) 1975 North Atlantic (Table 1). The focal mechanism for the 1975 event is from Lynnes and Ruff (1985). The number of aftershocks, *Na* (obs), with $M \geq 4.5$ within the indicated source depth (*H*) range over the 60 day window is indicated for each event, along with the ratio of *Na* (obs)/*Na* (pred) using the reference model discussed in the text. The GCMT centroid depth of the mainshock is shown next to the event focal mechanism.

1975 Azores (M_S 7.9) (Figure 7c) (e.g., Lynnes & Ruff, 1985) earthquakes, all of which have relatively simple aftershock sequences (the 1983 Chagos aftershocks are quite productive as apparent in Figure 7b and Table 1) and occurred close to ridge or strike-slip transform plate boundaries (Lay, 2019). The 2004
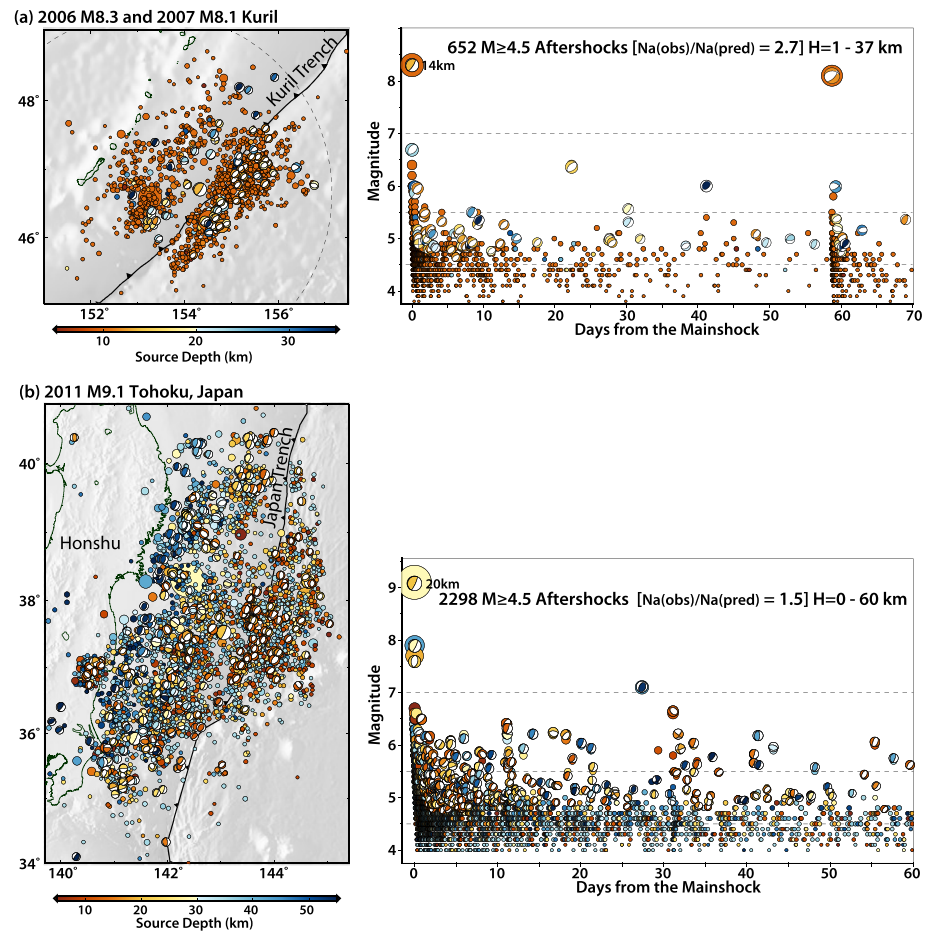
Figure 8. Complex earthquake sequences in old ocean lithosphere following great plate boundary thrust events in map view and as time series showing 70 or 60 day intervals of all seismicity from the USGS-NEIC catalog and all GCMT moment tensor solutions (both colored by source depth and scaled proportional to magnitude) within a two source dimension radius (dashed white lines are one source dimension radii) from each sequence mainshock for (a) 2006–2007 Kuril Islands Doublet and (b) 2011 Tohoku earthquake. The number of aftershocks, *Na* (obs), with $M \geq 4.5$ within the indicated source depth (*H*) range over the 70 or 60 day window is indicated for each event, along with the ratio *Na* (obs)/*Na*(pred) from Table 1. The GCMT centroid depth of the mainshock is shown next to the event focal mechanism.

Macquarie rupture has some directivity and possibly some along-strike segmentation. The smaller intraplate events in the Antarctic Plate (2015, M_W 7.1), Indian Plate (1999, M_W 7.0), and South of Australia (2001, M_W 7.1) all have minor aftershock sequences (Table 1) and no clear indication of multiple-faulting complexity, but their small size makes it hard to evaluate these events.

2.5. Great Interplate Thrust Events Producing Outer Trench Slope Sequences

Great megathrust earthquakes are commonly followed by oceanic intraplate earthquake sequences beneath the outer trench slope, sometimes extending to the outer rise. The most notable recent examples are the 2006 M_W 8.3 Kuril and 2011 M_W 9.1 Tohoku earthquakes (Table 1), which activated extensive faulting in the outer trench slope region initiating within minutes of the thrust event (Figure 8). The GCMT mechanisms indicate that in both cases this involved predominantly normal faulting with tension axes directed toward the trench. While there are many more examples of outer trench slope tensional faulting after large interplate events (e.g., Christensen & Ruff, 1988; Craig et al., 2014; Lay et al., 1989; Sladen & Trevisan, 2018), the extent of Pacific plate fracturing during these two events is quite remarkable. The 15 November 2006 Kuril mainshock (M_W 8.3) was followed by the 13 January 2007 M_W 8.1 outer trench slope normal faulting event (Figure 8a) (e.g., Ammon et al., 2008; Lay et al., 2009; Raeesi & Atakan, 2009; Tanioka et al., 2008). It appears that

multiple outer trench slope normal faults failed during the sequence. The 11 March 2011 Tohoku (M_W 9.1) rupture activated trench slope normal faulting as large as M_W 7.7 within 45 minutes of the mainshock (e.g., see many references in the review by Lay [2018]) but even more impressive is the swath of intraplate activity up to 150 km wide seaward of the Japan trench that ruptured within 60 days along a 400 km length of the subduction zone (Figure 8b). In these cases, along with many other examples discussed by Sladen and Trevisan (2018), the near-trench oceanic lithosphere can experience widespread fracturing during the transient stresses following interplate failure, which is superimposed on the plate bending stresses from slab pull. There are multiple pairs of major interplate thrust and major outer trench slope normal fault events with quite productive aftershock sequences separated by weeks to months in the Loyalty Islands, Vanuatu, and Solomon Islands, indicating strong temporal interactions for smaller mainshocks in the magnitude range 7.0 to 7.7.

2.6. Complex Sequences Near Subduction Zone Corners

Complex fracturing of oceanic lithosphere also occurs in sequences involving both interplate and intraplate ruptures near corners of subduction zones (Figure 9). These examples, all of which have high aftershock productivity (Table 1), are distinct from the 2018 Nikol'skoye sequence near a plate boundary corner, in that they directly involve substantial interplate thrusting. The 2000 New Ireland event commenced with a M_W 8.0 strike-slip event along the boundary between the Bismark and Pacific plates (Figure 9a), which activated two large M_W 7.9 thrust aftershocks in the New Britain trench, where the Solomon Sea plate subducts toward the northwest, along with numerous intraplate events with diverse faulting mechanisms in the adjacent plates (e.g., Geist & Parsons, 2005; Park & Mori, 2007). The Solomon Sea plate distorts around a 90° bend and also underthrusts the Pacific plate along the Solomon trench.

The 2009 Samoa M_W 8.1 event (Figure 9b) began with an outer rise normal fault rupture that triggered magnitude 8 thrust faulting on the Tonga megathrust to the south (e.g., Beavan et al., 2010; Fan et al., 2016; Lay et al., 2010). While the fracturing of the outer rise appears to have been localized near the corner in the Tonga subduction zone where the Pacific plate is tearing (Figure 8b), the overall sequence extended into the upper plate over hundreds of kilometers.

The 2013 Santa Cruz Islands earthquake sequence (Figure 9c) involved an M_W 8.0 thrust event at the northern end of the Vanuatu subduction zone, preceded and followed by extensive intraplate rupturing in the upper Pacific plate and the underthrusting Australian plate (e.g., Hayes et al., 2014; Heidarzadeh et al., 2016; Lay et al., 2013). The 90° corner of the plate boundary connects thrust faulting along the Vanuatu arc to strike-slip faulting extending to the west. The diversity and aftershock productivity of this sequence, with many intraplate events in the Pacific plate, is substantial.

3. Oceanic Plate Boundary Strike-Slip Sequences Away From Ridges

Oceanic transform faulting has been extensively studied, with relatively simple ruptures that may have some along-strike segmentation and relatively low aftershock productivity (e.g., Abercrombie & Ekström, 2003; Boettcher & Jordan, 2004). We consider additional major sequences along oceanic strike-slip boundaries well removed from spreading ridges, as demonstrated for the 2013 Craig, Alaska (M_W 7.5) (e.g., Yue et al., 2013) and 2017 Komandorksy Islands (M_W 7.7) (e.g., Lay et al., 2017) ruptures (Figure 10). The latter sequences, which rupture on very straight plate boundary segments, have relatively low aftershock productivity (Table 1) and minor diversity in faulting mechanisms.

4. Summary of Observed Complexity

The diversity of oceanic intraplate earthquake sequences is hard to address with quantitative modeling, but the observations discussed in this paper suggest a degree of common behavior in distinct tectonic configurations. Our operational definition of complexity is with respect to activation of multiple fault segments with diverse orientations during the mainshock rupture and/or aftershock sequence. All large earthquakes tend to have some slip heterogeneity and many include along-strike rupture of similarly oriented segments, but those attributes are not emphasized in our definition. Given that most events of interest here are remote and our primary information is from teleseismic signals, we focus our attention on the larger intraplate events ($M_W \geq 7.3$, and mostly ≥ 7.7) away from plate boundaries (> ~30–100 km); smaller events are hard
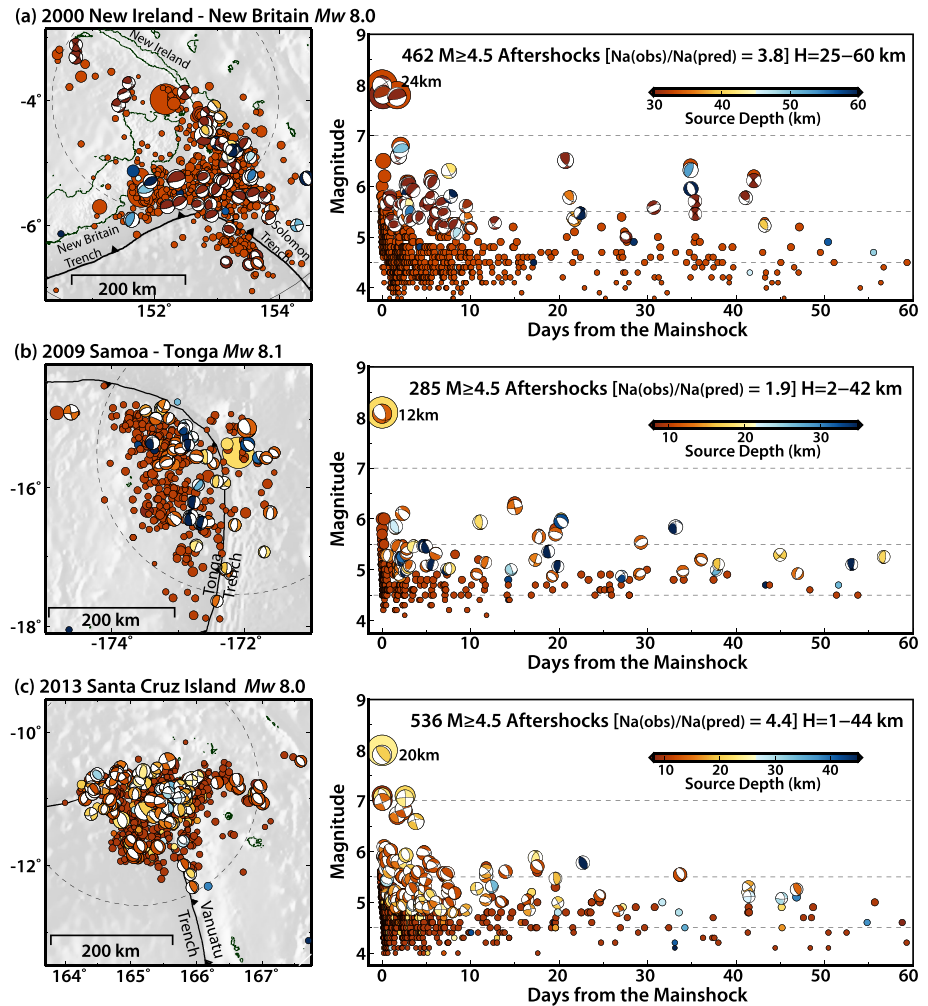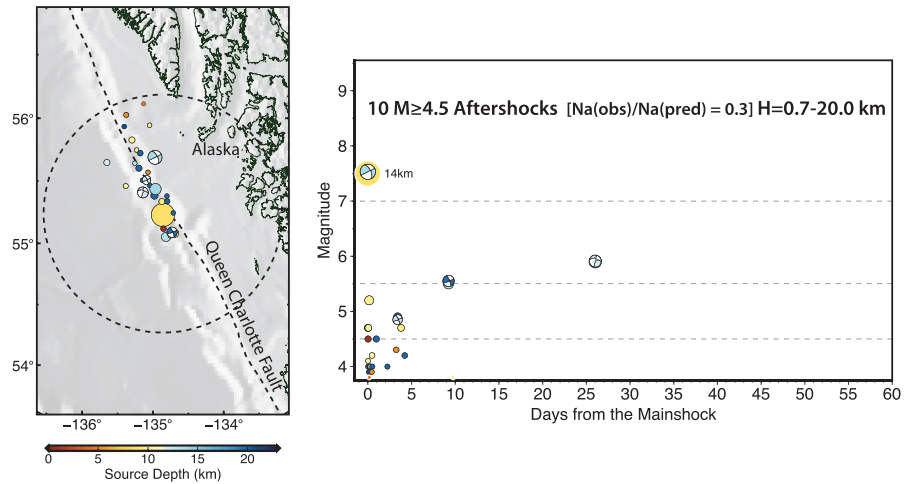
Figure 9. Complex earthquake sequences near sharp corners in subduction zones in map view and as time series showing 60 day intervals of all seismicity from the USGS-NEIC catalog and all GCMT moment tensor solutions (both colored by source depth and scaled proportional to magnitude) within a two source dimension radius (dashed white lines are one source dimension radii, and solid white lines are two source dimensions) from each sequence mainshock for (a) 2000 New Ireland-New Britain, (b) 2009 Samoa-Tonga, and (c) 2013 Solomon-Santa Cruz Island. The number of aftershocks, Na (obs), with $M \geq 4.5$ within the indicated source depth (H) range over the 60 day window is indicated for each event, along with the ratio Na (obs)/Na (pred) from Table 1. The GCMT centroid depth of the mainshock is shown next to the event focal mechanism.

to evaluate for our complexity characteristics. Given the low occurrence rate of major intraplate sequences in oceanic lithosphere, generalizations must be tentative, and we do not strive for quantitative models at this time. Figure 11 schematically summarizes the pertinent observations at present. While it is possible that all of the complex sequences arise from very localized, regionally specific conditions, the consistency of the behavior at least raises the possibility of some common controlling factors.

We relate the complex sequences in relatively old oceanic lithosphere seaward of the outer trench slope (Figures 4 and 5) with lateral and/or temporal stress gradients along the subduction/convergence zone. The occurrence of major strike-slip faulting as for the 1987–1988 Gulf of Alaska, 2012 Indo-Australia, and 2018 Off-Kodiak events is associated with strong lateral large-scale variations in temporal and spatial interplate coupling. The great interplate 1964 Alaska and 2004 Sumatra earthquakes preceded these events, with broad regions of time-varying elastic and viscoelastic loading of the seaward plate by bending and postseismic deformation producing horizontal tension axes in the direction of subduction. But these regions also have large-scale collisional processes occurring along the strike of the subduction zone, with the Indian
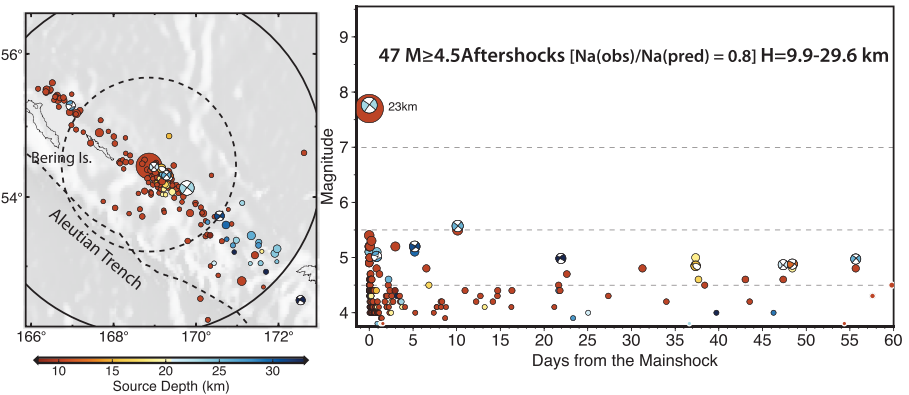
Figure 10. Large oceanic strike-slip earthquake sequences in oceanic lithosphere in map view and as time series showing 60 day intervals of all seismicity from the USGS-NEIC catalog and all GCMT moment tensor solutions (both colored by source depth and scaled proportional to magnitude) within a two source dimension radius (dashed white lines are one source dimension radii, and solid white lines are two source dimensions) from each sequence mainshock for (a) 2013 Craig, Alaska, and (b) 2017 Komandorsky Islands (Western Aleutians) along the Bering Fracture Zone. The number of aftershocks, Na (obs), with $M \geq 4.5$ within the indicated source depth (H) range over the 60 day window is indicated for each event, along with the ratio of Na (obs)/Na (pred) using the reference model discussed in the text. The GCMT centroid depth of the mainshock is shown next to the event focal mechanism.

continental collision west of the 2012 sequence and the Yakutat terrane collision north and east of the 1987–1988 and 2018 sequences. These collisions induce horizontal principal stress directions in the oceanic lithosphere that combine with slab pull stresses to give rise to strike-slip faulting patterns over broad intraplate regions from the subduction zone to well offshore. For the Indo-Australia plate, the development of the broad intraplate deformation zone extending from the Ninetyeast ridge to the Wharton basin, extending into the outer trench slope region along Sumatra and Nicobar, reflects the thousands of kilometers scale of the variation from continental collision to island arc subduction along the margin of the Indo-Australian plate (e.g., Coblentz et al., 1998; Stevens et al., 2020). Combined with the thermal thickening of relatively old oceanic lithosphere, which deepens the seismogenic layer (e.g., Aderhold & Abercrombie, 2016; Lay, 2019), the regional stress regimes load the oceanic lithosphere extensively, with broad areas accumulating stress and then failing with large multifault ruptures of diverse faulting orientations and large scale "macrofracturing" of a distributed network of faults failing in extensive aftershocks. We adapt this terminology from rock physics experiments, in which spatially distributed microfracturing with variable mechanism occurs in intact rock prior to localization in through-going faults (e.g., Mogi, 1962; Scholz, 1968).
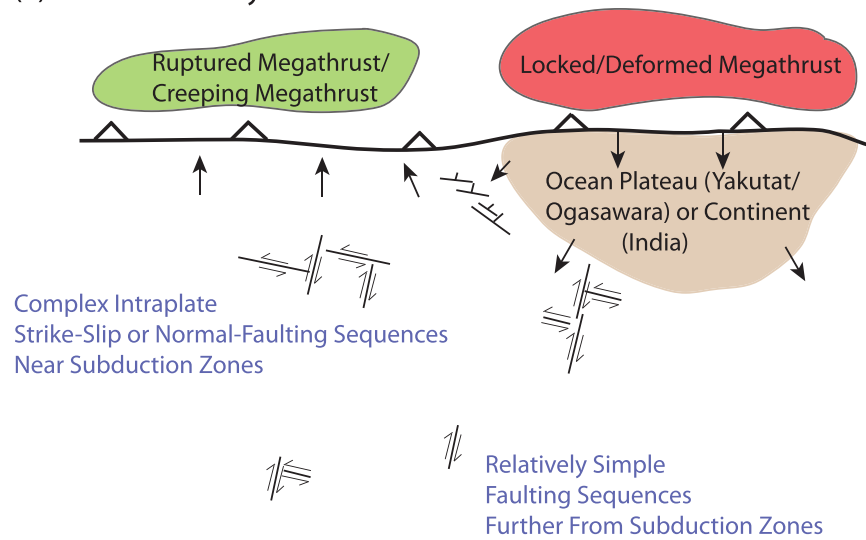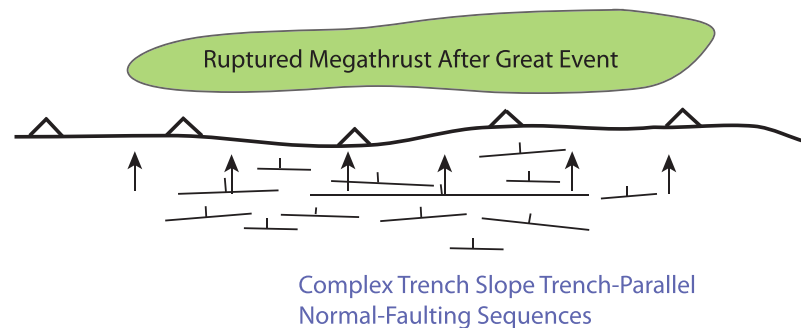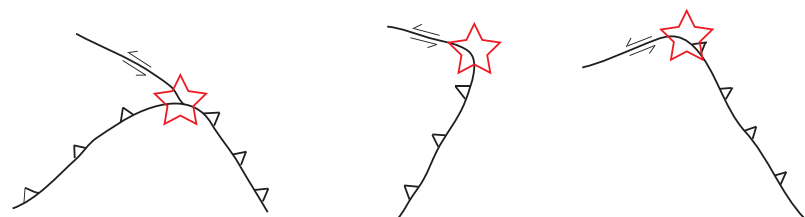
Figure 11. Tectonic scenarios giving rise to complex intraplate sequences in oceanic lithosphere. (a) Laterally varying stress along subduction zones arising from convergence of oceanic plateaus or continental material adjacent to oceanic convergent zone that have strong slab pull and large earthquake cycles give rise to complex strike-slip sequences seaward of the outer rise (Figures 4b–4d and 5) or complex obliquely trending normal fault sequences near the trench (Figure 4a) and less complex strike-slip sequences further from the boundary (Figure 6). (b) Slab bending stresses driven by slab pull, modulated by earthquake cycle stresses activate multiple normal-fault systems in the outer trench slope and outer rise (Figure 7). (c) Sharp corners in subduction zones associated with slab draping (left), lithospheric tearing (middle), and slab edges (right), produce complex sequences with interplate and intraplate faulting, which can extend into old oceanic lithosphere (Figure 8).

Some fossil fracture zones tend to control failure of major intraplate ruptures close to transform boundaries (e.g., Bohnenstiehl et al., 2004; Robinson, 2011), but this is not clearly a dominant factor in older oceanic lithosphere, as the 1987–1988, 2012, and 2018 sequences all have primary ruptures at large angles to fracture zone structures and the overall seismicity is not clearly aligned on fossil structures. Ridge-parallel dipping normal-faulting fabric could serve to localize faulting at high angles to fossil transforms, but the steeply dipping planes of the observed sequences do not clearly track such fabric either. Thus, much of the large seismicity in oceanic lithosphere just seaward of the outer trench slope appears to involve formation and/or growth of immature faults.

The 2010 Ogasawara and 2018 Nikol'skoye events are not temporally linked to nearby giant megathrust failures, but in both cases, there is strong lateral gradient in bathymetric structure in very old oceanic lithosphere impinging on the trench; the Ogasawara Plateau and track of the Hawaiian-Emperor hotspot (Figure 1) are adjacent to these ruptures, respectively. The Bonin subduction zone has no history of great interplate ruptures and may be very weakly coupled. The oblique trend of the 2010 sequence relative to the Plateau and the subduction zone is close to the trajectory of an old fracture zone, but deformation is not concentrated on that fossil structure and the plate experiences distributed macrofracturing. The Kamchatka margin near the Nikol'skoye event does have a history of major thrust events including those in 1923 (M_W 8.4) and 1997 (M_W 7.8), and the Komandorsky sliver, which is largely captured by the Pacific plate, is colliding with the Kamchatka continental lithosphere just to the north near the 1917 (M_W 7.9) and 1971 (M_W 7.6) events, so strong lateral gradients in plate boundary stress may account for the oblique geometry of the faulting in the northwesternmost Pacific plate.

While major event sequences do occur within oceanic plates further from plate boundaries, the available examples (Figures 6 and 7) tend to be more localized and less complex in terms of nonaligned mainshock faults and extensive aftershock sequences being activated. This suggests that proximity to the plate boundary spatiotemporal stress gradient conditions plays a role in bringing broadly distributed regions close to failure so that complex macrofracturing sequences accompany major earthquakes. This notion is supported by the activation of distributed outer trench slope and outer rise sequences following great interplate ruptures (Figure 11b), as displayed in the sequences following the 2006 M_W 8.3 Kuril and 2011 M_W 9.1 Tohoku earthquakes (Figure 8), where the predominantly two-dimensional time-varying plate boundary stress conditions favor extensional faulting. Flexure of the lithosphere as the incoming plate bends produces distributed loading of many weaknesses in the plate that can macrofracture in response to the abrupt lowering of compressional stress when the boundary fails. This outer trench slope environment can sometimes experience great localized decoupling extensional faulting, as in the case of the 1933 M_W 8.6 Sanriku and 1977 M_W 8.3 Sumba normal-faulting events, but such localized events appear to be rare and occur in regions of weak seismic coupling that lack boundary stress cycles.

The influence of laterally varying plate boundary stress conditions is further supported by the complex interplate/intraplate sequences near sharp subduction zone corners (Figure 11c). The intrinsically three-dimensional stress gradient expected for such contorted plate boundaries manifests in the high productivity, complex multifaulting sequences that occur close to the boundaries in these environments, as in the cases of the 2000 M_W 8.0 New Ireland, 2009 M_W 8.1 Samoa, and 2013 M_W 8.0 Santa Cruz Islands sequences (Figure 9).

All of the scenarios in Figure 11 have in common large-scale time-varying and spatially varying stress gradients spanning regions from hundreds to thousands of kilometers in length. The laterally varying boundary conditions may take the form of locking variations (11a and 11b) or sharp turns (11c). These large-scale plate boundary stress variations appear to allow fracturing over a large region, rather than localized on a single plane, with gradients of internal plate structure such as spreading fabrics, fracture zones, aseismic oceanic ridges, and oceanic plateaus concentrating the intraplate response into distributed deformation zones. Having broad regions loaded by the spatially varying stress in the plate abets critical stressing of many conjugate and nonoptimally oriented faults, so that complex faulting occurs. It is likely that dynamic triggering is enhanced in this environment, augmenting multifault rupture and widespread aftershock activity. Distributed faulting under even two-dimensional transient stress loading is demonstrated by the megathrust-faulting triggered sequences, and the broad reach of plate boundary geometry is demonstrated by the complex sequences around corners in subduction zones. In contrast, long straight oceanic plate

boundaries fail in relatively simple sequences. The observations suggest an important future approach to understanding earthquake complexity is to model or measure the requisite stress gradients giving rise to the qualitatively distinct behavior. However, quantifying each sequence will require regionally specific interactions of time-varying plate boundary stresses, bathymetric stresses and dynamic and static stress interactions when regions rupture.

5. Conclusions

Oceanic lithosphere of relatively large age that has strong laterally varying stress conditions on the plate boundary tends to experience infrequent very complex faulting or macrofracturing sequences over distributed regions seaward of the trench. Transient stress conditions from interplate earthquake cycles can modulate slab pull stresses to induce distributed extensional failures in the outer trench slope and outer rise, but slab pull stresses can also combine with compressional stresses from continental, oceanic plateau, or hotspot ridge collisions to favor strike-slip or oblique-faulting sequences within the oceanic lithosphere along strike from the collision zone. The most complex sequences occur just seaward of the outer trench slope, and many faults activate either coseismically in compound ruptures or are triggered efficiently by mainshock signals, producing widely distributed sequences. Major earthquakes farther from the plate boundary tend to be rare and rupture in less complex sequences.

Data Availability Statement

All broadband seismic waveforms used in this study were accessed from the Data Management Center of the Incorporated Research Institutions for Seismology (https://www.iris.edu/hq/). Centroid moment-tensor solutions were obtained from https://www.globalcmt.org/. Ocean bathymetry model ETOPO1 was obtained from NOAA (https://www.ngdc.noaa.gov/mgg/global/). The least squares inversion software is adapted from the package of Kikuchi and Kanamori (http://wwweic.eri.u-tokyo.ac.jp/ETAL/KIKUCHI/).

References

Abercrombie, R. E., Antolik, M., & Ekström, G. (2003). The June 2000 M_W 7.9 earthquakes south of Sumatra: Deformation in the India-Australia Plate. *Journal of Geophysical Research*, *108*(B1), 2018. https://doi.org/10.1029/2001JB000674

Abercrombie, R. E., & Ekström, G. (2003). A reassessment of the rupture characteristics of oceanic transform earthquakes. *Journal of Geophysical Research*, *108*(B5), 2225. https://doi.org/10.1029/2001JB000814

Aderhold, K., & Abercrombie, R. E. (2016). Seismotectonics of a diffuse plate boundary: Observations off the Sumatra-Andaman trench. *Journal of Geophysical Research: Solid Earth*, *121*, 3462–3478. https://doi.org/10.1002/2015JB012721

Ammon, C. J., Kanamori, H., & Lay, T. (2008). A great earthquake doublet and seismic stress transfer cycles in the central Kuril Islands. *Nature*, *451*(7178), 561–565. https://doi.org/10.1038/nature06521

Antolik, M., Kaverina, A., & Dreger, D. (2000). Compound rupture of the great 1998 Antarctic plate earthquake. *Journal of Geophysical Research*, *105*(B10), 23,825–23,838. https://doi.org/10.1029/2000JB900246

Beavan, J., Wang, X., Holden, C., Wilson, K., Power, W., Prasetya, G., et al. (2010). Near-simultaneous great earthquakes at Tongan megathrust and outer rise in September 2009. *Nature*, *466*(7309), 959–963. https://doi.org/10.1038/nature09292

Boettcher, M. S., & Jordan, T. H. (2004). Earthquake scaling relations for mid-ocean ridge transform faults. *Journal of Geophysical Research*, *109*, B12302. https://doi.org/10.1029/2004JB003110

Bohnenstiehl, D. R., Tolstoy, M., & Chapp, E. (2004). Breaking into the plate: A 7.6 M_W fracture-zone earthquake adjacent to the Central Indian Ridge. *Geophysical Research Letters*, *31*, L02615. https://doi.org/10.1029/2003GL018981

Boneh, Y., Schotenfels, E., Kwong, K., van Zelst, I., Tong, X., Limer, M., et al. (2019). Intermediate-depth earthquakes controlled by incoming plate hydration along bending-related faults. *Geophysical Research Letters*, *46*, 3688–3697. https://doi.org/10.1029/2018GL081585

Christensen, D. H., & Ruff, L. J. (1988). Seismic coupling and outer-rise earthquakes. *Journal of Geophysical Research*, *93*(B11), 13,421–13,444. https://doi.org/10.1029/JB093iB11p13421

Coblentz, D. D., Zhou, S., Hillis, R. R., Richardson, R. M., & Sandiford, M. (1998). Topography, boundary forces, and the Indo-Australian intraplate stress field. *Journal of Geophysical Research*, *103*(B1), 919–931. https://doi.org/10.1029/97JB02381

Craig, T. J., Copley, A., & Jackson, J. (2014). A reassessment of outer-rise seismicity and its implications for the mechanics of oceanic lithosphere. *Geophysical Journal International*, *197*(1), 63–89. https://doi.org/10.1093/gji/ggu013

Dascher-Cousineau, K., Brodsky, E. E., Lay, T., & Goebel, T. H. W. (2020). What controls variations in aftershock productivity? *Journal of Geophysical Research: Solid Earth*, *125*, e2019JB01811. https://doi.org/10.1029/2019JB01811

Delescluse, M., Chamot-Rooke, N., Cattin, R., Fleitout, L., Trubienko, O., & Vigny, C. (2012). April 2012 intra-oceanic seismicity off Sumatra boosted by the Banda-Aceh megathrust. *Nature*, *490*(7419), 240–244. https://doi.org/10.1038/nature11520

Duputel, Z., Kanamori, H., Tsai, V. C., Rivera, L., Meng, L., Ampuero, J.-P., & Stock, J. M. (2012). The 2012 Sumatra great earthquake sequence. *Earth and Planetary Science Letters*, *351–352*, 247–257. https://doi.org/10.1016/j.epsl.2012.07.017

Faccenda, M., Gery, T. V., & Burlini, L. (2009). Deep slab hydration induced by bending-related variations in tectonic pressure. *Nature Geoscience*, *2*(11), 790–793. https://doi.org/10.1038/ngeo656

Fan, W., Shearer, P. M., Ji, C., & Bassett, D. (2016). Multiple branching rupture of the 2009 Tonga-Samoa earthquake. *Journal of Geophysical Research: Solid Earth*, *121*, 5809–5827. https://doi.org/10.1002/2016JB012945

Hayes, G. P., Frulong, K. P., & Ammon, C. J. (2009). Intraplate deformation adjacent to the Macquarie Ridge south of New Zealand: The tectonic evolution of a complex plate boundary. *Tectonophysics*, *463*, 14–14. https://doi.org/10.1016/j.tecto.2008.09.024

Geist, E. L., & Parsons, T. (2005). Triggering of tsunamigenic aftershocks from large strike-slip earthquakes: Analysis of the November 2000 New Ireland earthquake sequence. *Geochemistry, Geophysics, Geosystems*, *6*, Q10005. https://doi.org/10.1029/2005GC000935

Gusman, A. R., Satake, K., & Harada, T. (2017). Rupture process of the 2016 Wharton Basin strike-slip faulting earthquake estimated from joint inversion of teleseismic and tsunami waveforms. *Geophysical Research Letters*, *44*, 4082–4089. https://doi.org/10.1002/2017GL073611

Hartzell, S. H., & Heaton, T. H. (1983). Inversion of strong ground motion and teleseismic waveform data for the fault rupture history of the 1979 Imperial Valley, California, earthquake. *Bulletin of the Seismological Society of America*, *73*(6A), 1553–1583.

Hayes, G. P., Furlong, K. P., Benz, H. M., & Herman, M. W. (2014). Triggered aseismic slip adjacent to the 6 February 2013 M_W 8.0 Santa Cruz Islands megathrust earthquake. *Earth and Planetary Science Letters*, *388*, 265–272. https://doi.org/10.1016/j.epsl.2013.11.010

Heidarzadeh, M., Harada, T., Satake, K., Ishibe, T., & Gusman, A. R. (2016). Comparative study of two tsunamigenic earthquakes in the Solomon Islands: 2015 M_W 7.0 normal-fault and 2013 Santa Cruz M_W 8.0 megathrust earthquakes. *Geophysical Research Letters*, *43*, 4340–4349. https://doi.org/10.1002/2016GL068601

Henry, C., Das, S., & Woodhouse, J. H. (2000). The great March 25, 1998, Antarctic Plate earthquake: Moment tensor and rupture history. *Journal of Geophysical Research*, *105*(B7), 16,097–16,118. https://doi.org/10.1029/2000JB900077

Hill, E. M., Yue, H., Barbot, S., Lay, T., Tapponnier, P., Hermawan, I., et al. (2015). The 2012 M_W 8.6 Wharton Basin sequence: A cascade of great earthquakes generated by near-orthogonal, young, oceanic-mantle faults. *Journal of Geophysical Research: Solid Earth*, *120*, 3723–3747. https://doi.org/10.1002/2014JB011703

Hjörleifsdóttir, V., Kanamori, H., & Tromp, J. (2009). Modeling 3D wave propagation and finite slip for the 1998 Balleny Islands earthquake. *Journal of Geophysical Research*, *114*, B03301. https://doi.org/10.1029/2008JB005975

Hossen, M. J., Sheehan, A. F., & Satake, K. (2020). A multi-fault model estimation from tsunami data: An application to the 2018 M7.9 Kodiak earthquake. *Pure and Applied Geophysics*, *177*(3), 1335–1346. https://doi.org/10.1007/s00024-020-02433-z

Hwang, L. J., & Kanamori, H. (1992). Rupture processes of the 1987–1988 Gulf of Alaska earthquake sequence. *Journal of Geophysical Research*, *97*(B13), 19,881–19,908. https://doi.org/10.1029/92JB01817

Ishii, M., Kiser, E., & Geist, E. L. (2013). M_W 8.6 Sumatran earthquake of 11 April 2012: Rare seaward expression of oblique subduction. *Geology*, *41*(3), 319–322. https://doi.org/10.1130/G33783.1

Kennett, B. L. N., Gorbatov, A., & Spiliopoulos, S. (2014). Tracking high-frequency seismic source evolution: 2004 M_W 8.1 Macquarie event. *Geophysical Research Letters*, *41*, 1187–1193. https://doi.org/10.1002/2013GL058935

Kikuchi, M., & Kanamori, H. (1991). Inversion of complex body waves—III. *Bulletin of the Seismological Society of America*, *81*(6), 2335–2350.

Kogan, M. G., Frolov, D. I., Vasilenko, N. F., Freymueller, J. T., Steblov, G. M., Ekström, G., et al. (2017). Plate coupling and strain in the far western Aleutian arc modeled from GPS data. *Geophysical Research Letters*, *44*, 3176–3183. https://doi.org/10.1002/2017GL072735

Krabbenhoeft, A., von Huene, R., Miller, J. J., Lange, D., & Vera, F. (2018). Strike-slip 23 January 2018 M_W 7.9 Gulf of Alaska rare intraplate earthquake: Complex rupture of a fracture zone system. *Scientific Reports*, *8*, 13706. https://doi.org/10.1038/s41598-018-32071-4

Kuge, K., Kikuchi, M., & Yamanaka, Y. (1999). Non-double-couple moment tensor of the March 25, 1998, Antarctic earthquake: Composite for strike-slip and normal faults. *Geophysical Research Letters*, *26*(22), 3401–3404. https://doi.org/10.1029/1999GL005420

Yadav, R. K., Kundu, B., Gahalaut, K., Catherine, J., Gahalaut, V. K., Ambikapthy, A., & Naidu, M. S. (2017). Coseismic offsets due to the April 11, 2012 Indian Ocean earthquakes (M_W 8.6 and 8.2) derived from GPS measurements. *Geophysical Research Letters*, *40*, 3389–3393. https://doi.org/10.1002/grl.50601

Lahr, J. C., Page, R. A., Stephens, C. D., & Christensen, D. H. (1988). Unusual earthquakes in the Gulf of Alaska and fragmentation of the Pacific plate. *Geophysical Research Letters*, *18*, 1483–1486. https://doi.org/10.1029/GL015i013p01483

Lay, T. (2018). A review of the rupture characteristics of the 2011 Tohoku-oki M_W 9.1 earthquake. *Tectonophysics*, *733*, 4–36. https://doi.org/10.1016/j.tecto.2017.09.022

Lay, T. (2019). Reactivation of oceanic fracture zones in large intraplate earthquakes? In *Transform Plate Boundaries and Fracture Zones* (pp. 89–104). Amsterdam: J. C. Duarte, Elsevier. https://doi.org/10.1016/B978-0-12-812064-4.00004-9

Lay, T., Ammon, C. J., Kanamori, H., Rivera, L., Koper, K. D., & Hutko, A. R. (2010). The 2009 Samoa-Tonga great earthquake triggered doublet. *Nature*, *466*(7309), 964–968. https://doi.org/10.1038/nature09214

Lay, T., Astiz, L., Kanamori, H., & Christensen, D. H. (1989). Temporal variation of large intraplate earthquakes in coupled subduction zones. *Physics of the Earth and Planetary Interiors*, *54*(3–4), 258–312. https://doi.org/10.1016/0031-9201(89)90247-1

Lay, T., Ye, L., Bai, Y., Cheung, K. F., Kanamori, H., Freymueller, J., et al. (2017). Rupture along 400 km of the Bering Fracture Zone in the Komandorsky Islands Earthquake (M_W 7.8) of 17 July 2017. *Geophysical Research Letters*, *44*, 12,161–12,169. https://doi.org/10.1002/2017GL076148

Lay, T., Kanamori, H., Ammon, C. J., Hutko, A. R., Furlong, K., & Rivera, L. (2009). The 2006–2007 Kuril Islands great earthquake sequence. *Journal of Geophysical Research*, *114*, B113208. https://doi.org/10.1029/2008JB006280

Lay, T., Ye, L., Kanamori, H., Yamazaki, Y., Cheung, K. F., & Ammon, C. J. (2013). The February 6, 2013 M_W 8.0 Santa Cruz Islands earthquake and tsunami. *Tectonophysics*, *608*, 1109–1121. https://doi.org/10.1016/j.tecto.2013.07.001

Lay, T., Liu, C., & Kanamori, H. (2019). Enhancing tsunami warning using *P* wave coda. *Journal of Geophysical Research: Solid Earth*, *124*, 10,583–10,609. https://doi.org/10.1029/2019JB018221

Lay, T., Ye, L., Ammon, C. J., Dunham, A., & Koper, K. D. (2016). The 2 March 2016 Wharton Basin M_W 7.8 earthquake: High stress drop north-south rupture in the diffuse oceanic deformation zone between the Indian and Australian plates. *Geophysical Research Letters*, *43*, 7937–7945. https://doi.org/10.1002/2016GL069931

Lay, T., Ye, L., Bai, Y., Cheung, K. F., & Kanamori, H. (2018). The 2018 M_W 7.9 Gulf of Alaska earthquake: Multiple fault rupture in the Pacific plate. *Geophysical Research Letters*, *45*, 9542–9551. https://doi.org/10.1029/2018GL079813

Lynnes, C. S., & Ruff, L. J. (1985). Source process and tectonic implications of the great 1975 North Atlantic earthquake. *Geophysical Journal of the Royal Astronomical Society*, *82*(3), 497–510. https://doi.org/10.1111/j.1365-246X.1985.tb05148.x

Meng, L., Ampuero, J.-P., Stock, J., Duputel, Z., Luo, Y., & Tsai, V. C. (2012). Earthquake in a maze: Compressional rupture branching during the 2012 M_W 8.6 Sumatra earthquake. *Science*, *337*(6095), 724–726. https://doi.org/10.1126/science.1224030

Mogi, K. (1962). Study of the elastic shocks caused by the fracture of heterogeneous materials and its relation to earthquake phenomena. *Bulletin of the Earthquake Research Institute*, *40*, 125–173.

Nettles, M., Wallace, T. C., & Beck, S. L. (1999). The March 25, 1998 Antarctic plate earthquake. *Geophysical Research Letters*, *26*(14), 2097–2100. https://doi.org/10.1029/1999GL900387

Obana, K., Takahashi, T., No, T., Kaiho, Y., Kodaira, S., Yamashita, M., et al. (2014). Distribution and migration of aftershocks of the 2010 M_W 7.4 Ogasawara Islands intraplate normal-faulting earthquake related to a fracture zone in the Pacific plate. *Geochemistry, Geophysics, Geosystems*, *15*, 1363–1373. https://doi.org/10.1002/2014GC005246

Park, S.-C., & Mori, J. (2007). Triggering of earthquakes during the 2000 Papua New Guinea earthquake sequence. *Journal of Geophysical Research*, *112*, B03302. https://doi.org/10.1029/2006JB004480

Pegler, G., & Das, S. (1996). The 1987–1992 Gulf of Alaska earthquakes. *Tectonophysics*, *257*(2–4), 111–136. https://doi.org/10.1016/0040-1951(95)00112-3

Portnyagin, M., Savelyev, D., Hoernle, K., Hauff, F., & Garbe-Schönberg, D. (2008). Mid-Cretaceous Hawaiian tholeiites preserved in Kamchatka. *Geology*, *36*(11), 903–906. https://doi.org/10.1130/G2517A.1

Quintanar, L., Madariaga, R., & Deschamps, A. (1995). The earthquake sequence of November 1987 and March 1988 in the Gulf of Alaska: A new insight. *Geophysical Research Letters*, *22*(9), 1029–1032. https://doi.org/10.1029/95GL00905

Raeesi, M., & Atakan, K. (2009). On the deformation cycle of a strongly coupled plate interface: the triple earthquakes of 16 March 1963, 15 November 2006, and 13 January 2007 along the Kurile subduction zone. *Journal of Geophysical Research*, *114*, B10301. https://doi.org/10.1029/2008JB006184

Ranero, C. R., Morgan, J. P., McIntosh, K., & Reichert, C. (2003). Bending-related faulting and mantle serpentinization at the Middle America trench. *Nature*, *425*(6956), 367–373. https://doi.org/10.1038/nature01961

Robinson, D. P. (2011). A rare great earthquake on an oceanic fossil fracture zone. *Geophysical Journal International*, *186*(3), 1121–1134. https://doi.org/10.1111/j.1365-246X.2011.05092.x

Robinson, D. P., Henry, C., Das, S., & Woodhouse, J. H. (2001). Simultaneous rupture along two conjugate planes of the Wharton Basin earthquake. *Science*, *292*(5519), 1145–1148. https://doi.org/10.1126/science.1059395

Ruppert, N. A., Rollins, C., Zhang, A., Meng, L., Holtkamp, S. G., West, M. E., & Freymueller, J. T. (2018). Complex faulting and triggered rupture during the 2018 M_W 7.9 offshore Kodiak, Alaska, earthquake. *Geophysical Research Letters*, *45*, 7533–7541. https://doi.org/10.1029/2018GL078931

Satriano, C., Kiraly, E., Bernard, P., & Vilotte, J.-P. (2012). The 2012 M_W 8.6 Sumatra earthquake: Evidence of westward sequential seismic ruptures associated to the reactivation of a N-S ocean fabric. *Geophysical Research Letters*, *39*, L15302. https://doi.org/10.1029/2012GL052387

Scholz, C. H. (1968). The frequency-magnitude relation of microfracturing in rock and its relation to earthquakes. *Bulletin of the Seismological Society of America*, *58*, 399–415.

Singh, S. C., Hananto, N., Qin, Y., Leclerc, F., Avianto, P., Tapponnier, P. E., et al. (2017). The discovery of a conjugate system of faults in the Wharton Basin intraplate deformation zone. *Science Advances*, *3*, e1601689. https://doi.org/10.1126/sciadv.1601689

Sladen, A., & Trevisan, J. (2018). Shallow megathrust earthquake ruptures betrayed by their outer-trench aftershock signature. *Earth and Planetary Science Letters*, *483*, 105–113. https://doi.org/10.1016/j.epsl.2017.12.006

Stevens, D. E., McNeill, L. C., Henstock, T. J., Delescluse, M., Chamot-Rooke, N., & Bull, J. M. (2020). A complete structural model and kinematic history for distributed deformation in the Wharton Basin. *Earth and Planetary Science Letters*, *538*, 116218. https://doi.org/10.1016/j.epsl.2020.116218

Tanioka, Y., Hasegawa, Y., & Kuwayama, T. (2008). Tsunami waveform analyses of the 2006 underthrust and 2007 outer-rise Kurile earthquakes. *Advances in Geosciences*, *14*, 129–134. https://doi.org/10.5194/adgeo-14-129-2008

Tsuboi, S., Kikuchi, M., Yamanaka, Y., & Kanao, M. (2000). The March 25, 1998 Antarctic earthquake: Great earthquake caused by post-glacial rebound. *Earth, Planets and Space*, *52*(2), 133–136. https://doi.org/10.1186/BF03351621

Wang, D., Mori, J., & Uchide, T. (2012). Supershear rupture on multiple faults for the M_W 8.6 Off Northern Sumatra, Indonesia earthquake of April 11, 2012. *Geophysical Research Letters*, *39*, L21307. https://doi.org/10.1029/2012GL053622

Wang, K., Thomson, R. E., Rabinovich, A. B., Fine, I. V., & Insua, T. L. (2020). The 2018 Alaska-Kodiak tsunami off the west coast of North America: A rare mid-plate tsunamigenic event. *Pure and Applied Geophysics*, *177*(3), 1347–1378. https://doi.org/10.1007/s00024-020-02427-x

Wei, S., Helmberger, D., & Avouac, J.-P. (2013). Modeling the 2012 Wharton basin earthquakes off-Sumatra: Complete lithospheric failure. *Journal of Geophysical Research: Solid Earth*, *118*, 3592–3609. https://doi.org/10.1002/jgrb.50267

Wells, D. L., & Coppersmith, K. J. (1994). New empirical relationships among magnitude, rupture length, rupture width, rupture area, and surface displacement. *Bulletin of Seismological Society of America*, *84*(4), 974–1002.

Wen, Y., Guo, Z., Xu, C., Xu, G., & Song, C. (2019). Coseismic and postseismic deformation associated with the 2018 M_W 7.8 Kodiak, Alaska, earthquake from low-rate and high-rate GPS observations. *Bulletin of the Seismological Society of America*, *109*(3), 908–918. https://doi.org/10.1785/0120180246

Wetzler, N., Lay, T., Brodsky, E. E., & Kanamori, H. (2017). Rupture-depth-varying seismicity patterns for major and great ($M_W \geq 7.0$) megathrust earthquakes. *Geophysical Research Letters*, *44*, 9663–9671. https://doi.org/10.1002/2017GL074573

Wiens, D. A., & Stein, S. (1984). Intraplate seismicity and stresses in young oceanic lithosphere. *Journal of Geophysical Research*, *89*(B13), 11,442–11,464. https://doi.org/10.1029/JB089iB13p11442

Wiens, D. A., DeMets, C., Gordon, R. G., Stein, S., Argus, D., Engeln, J. F., et al. (1985). A diffuse plate boundary model for Indian Ocean tectonics. *Geophysical Research Letters*, *12*(7), 429–432. https://doi.org/10.1029/GL012i007p00429

Wiseman, K., & Bürgmann, R. (2012). Stress triggering of the great Indian Ocean strike-slip earthquakes in a diffuse plate boundary zone. *Geophysical Research Letters*, *39*, L22304. https://doi.org/10.1029/2012GL053954

Xu, Y., Koper, K. D., Sufri, O., Zhu, L., & Hutko, A. R. (2009). Rupture imaging of the M_W 7.9 12 May 2008 Wenchuan earthquake from back projection of teleseismic P waves. *Geochemistry, Geophysics, Geosystems*, *10*, Q04006. https://doi.org/10.1029/2008GC002335

Ye, L., Lay, T., & Kanamori, H. (2020). Anomalously low aftershock productivity of the 2019 M_W 8.0 energetic intermediate-depth faulting beneath Peru. *Earth and Planetary Science Letters*, in revision, *549*, 116528. https://doi.org/10.1016/j.epsl.2020.116528

Ye, L., Lay, T., Kanamori, H., & Rivera, L. (2016). Rupture characteristics of major and great ($M_W \geq 7.0$) megathrust earthquakes from 1990–2015: 1. Source parameter scaling relationships. *Journal of Geophysical Research: Solid Earth*, *121*, 826–844. https://doi.org/10.1002/2015JB012426

Yue, H., & Lay, T. (2020). Resolving complicated faulting process using multi-point-source representation: Iterative inversion algorithm improvement and application to recent complex earthquakes. *Journal of Geophysical Research: Solid Earth*, *125*, e2019JB018601. https://doi.org/10.1029/2019JB018601

Yue, H., Lay, T., Freymueller, J. T., Ding, K., Rivera, L., Ruppert, N. A., & Koper, K. D. (2013). Supershear rupture of the 5 January 2013 Craig, Alaska (M_W 7.5) earthquake. *Journal of Geophysical Research: Solid Earth*, *118*, 5903–5919. https://doi.org/10.1002/2013JB010594

Yue, H., Lay, T., & Koper, K. D. (2012). *En échelon* and orthogonal fault ruptures of the 11 April 2012 great intraplate earthquakes. *Nature*, *490*(7419), 245–249. https://doi.org/10.1038/nature11492

Zhang, H., Chen, J., & Ge, Z. (2012). Multi-fault rupture and successive triggering during the 2012 M_W 8.6 Sumatra offshore earthquake. *Geophysical Research Letters*, *39*, L22305. https://doi.org/10.1029/2012GL053805

Zhao, B., Qi, Y., Wang, D., Yu, J., Li, Q., & Zhang, C. (2019). Coseismic slip model of the 2018 M_W 7.9 Gulf of Alaska earthquake and its seismic hazard implications. *Seismological Research Letters*, *90*(2A), 642–648. https://doi.org/10.1785/0220180141

Macrofracturing of Oceanic Lithosphere in Complex Large Earthquake Sequences

Thorne Lay[1], Lingling Ye[2], Zhenbo Wu[1,3], and Hiroo Kanamori[4]

[1]Earth and Planetary Sciences Department, University of California, Santa Cruz, CA, USA. [2]Guangdong Provincial Key Lab of Geodynamics and Geohazards, School of Earth Sciences and Engineering, Sun Yat-sen University, Guangzhou, China. [3]College of Geophysics, Chengdu University of Technology, Chengdu, China. [4]Seismological Laboratory, California Institute of Technology, Pasadena, CA, USA.

Contents of this file

Figures S1 to S12
Text S1 to S2

Introduction

Twelve figures are provided to support the main text. These show detailed results for finite-fault inversions of the 2010 Ogasawara earthquake (Figure S1-S6) and the 2018 Nikol'skoye earthquake (Figures S7-S12). Two text blocks provide detailed discussion of the source modeling for these two events.

Text S1. Finite-faulting investigation of the 2010 Ogasawara M_W 7.4 event.

The GCMT solution for the 2010 mainshock has a predominantly normal faulting solution with best double-couple faulting geometries having strike, $\phi_1 = 110°$, dip $\delta_1 = 40°$, rake $\lambda_1 = -137°$; and $\phi_2 = 345°$, $\delta_2 = 64°$, $\lambda_2 = -58°$, for a centroid depth of 15.6 km. The USGS-NEIC hypocenter depth is 14 km, and a *W*-phase inversion from Duputel reported by USGS-NEIC has a seismic moment, $M_0 = 1.11 \times 10^{20}$ Nm (M_W 7.3) with best double-couple faulting geometries of $\phi_1 = 113°$, $\delta_1 = 46°$, $\lambda_1 = -131°$, and $\phi_2 = 345°$, $\delta_2 = 57°$, $\lambda_2 = -56°$ for a centroid depth of 25.5 km (https://earthquake.usgs.gov/earthquakes/eventpage/usp000hr97/executive). The overall 60-day aftershock distribution, elongated in the northwest-southeast direction with depths ranging from 1 to 20 km, and the associated GCMT focal mechanisms with centroid depths from 6 to 30 (Figure 2a) do not constrain a favored rupture plane, and cannot be reconciled with the sequence being confined to a single fault.

In order to place bounds on the rupture distribution for the event, we perform back-projections of short-period (0.5-2 s) and intermediate period (1-20 s) teleseismic *P* waves from large regional networks of stations in North America and Eurasia, along with a global network of stations (Figure S1). The short-period images indicate concentration of coherent *P* wave energy around the source epicenter, without consistent resolution of finiteness due to array response artifacts. The primary power in the stacked signals is concentrated within 20 s of the origin, with some energy persisting to about 30 s. These images are generally similar to IRIS back projections for short-period data of 0.25-1.0 Hz (http://ds.iris.edu/spud/backprojection/112339). The short-period back-projections do not provide robust constraint on source finiteness or rupture velocity, but do favor a spatially concentrated source region of the short-period radiation. However, our intermediate period images indicate the presence of moderate waveform power from 40 to 60 s after the rupture onset, with the images for all three networks indicating a secondary source location generally west of the plate boundary. Examination of profiles of broadband teleseismic *P* waveforms reveals clear ringing coda, persisting for as much as 150 s after the first arrival, indicative of water multiples (e.g., Lay et al., 2019). This is particularly evident at epicentral distances from 70° to 100° and is most coherent across North American stations.

We perform finite-fault slip inversions of teleseismic broadband *P* and *SH* waveforms for both candidate fault planes for the GCMT and *W*-phase geometries, along with many perturbations of those geometries, finding strike and dip of the faults to not be better resolved than ±10° relative to either candidate fault. A simple 1D velocity model based on model Crust2 with a uniform water layer 4.3 km deep (Laske et al., https://igppweb.ucsd.edu/~gabi/crust2.html) is used for the source region structure. Given the rough bathymetry, with azimuthally varying character relative to the source, incomplete modeling of coda phases is expected. The inversions consistently give slightly (a few percent) better residual waveform power reduction for the southeast

striking fault, and Figure S2 shows a corresponding inversion for $\phi = 113°$, $\delta = 46°$, adopted from the *W*-phase solution of Duputel reported by USGS-NEIC. This model is parameterized with 15 10-km-long subfaults along strike and six 7-km wide subfaults along dip, with the hypocenter set at 17 km. 74 broadband *P* waves with excellent azimuthal distribution and 57 broadband *SH* waves are included in the inversion. A kinematic rupture expansion velocity of 2.5 km/s is used, with subfault source time functions parameterized with 10 2-s rise-time triangles offset by 2-s each, allowing up to 22 s subfault durations. The 2.5 km/s expansion velocity is not well constrained by the data, but for corresponding subfault source time function parameterization we find very similar slip distributions for values from 2.0 to 3.5 km/s, so the overall slip model is relatively stable. The resulting slip model has a primary slip patch extending from 8 to 29 km, with peak slip of ~4.7 m, and a secondary shallow slip patch southeast of the hypocenter. This model has a slip-weighted average stress drop of 12 MPa (following the procedure in Ye et al., 2016), with individual subfault source time functions generally indicating simple, short duration radiation. The USGS-NEIC finite fault solution used a fault with strike of 116.3° and dip of 40.4°, and has a single slip patch with radius of ~12 km extending from ~5 to 25 km depth with central peak slip of ~3 m (https://earthquake.usgs.gov/earthquakes/eventpage/usp000hr97/finite-fault).

The moment-rate function is most reliable for the first 25 s, and is then followed by diminishing pulses about 10 s apart, which plausibly represent imperfectly modeled water reverberations mapping into the source. Comparison of the observations and predictions from this model (Figure S3) indeed shows that the first ~35 s of the *P* and *SH* signals are well modeled, but energy from 40 to 60 s into the waveforms is not fully accounted for. To further evaluate whether this coda energy may involve secondary faulting, we perform inversions varying the strike in 10° azimuth intervals, seeking any orientation of faulting that might account for azimuthal timing and waveform variations of the coda, without finding significant improvement to the overall fit. We also apply a multi-point source inversion (Yue & Lay, 2020) to extensive horizontal grids of possible source locations, finding some models with secondary sources ~40 s after onset west of the Bonin Trench in the vicinity of the long-period back-projection images in Figure S1, but the mechanisms and locations are unstable. While triggering of early aftershocks at some distance from the mainshock may be involved, more complete modeling of water multiples with 3D bathymetry models is required before ruling out complex propagation effects.

Results for an inversion using the alternate fault plane, with $\phi = 345°$, $\delta = 57°$ are presented in Figures S4 and S5. Coda arrivals at some azimuths are accounted for slightly better, but overall the waveform misfit is slightly larger for this geometry. The overall distribution of aftershocks is clearly oblique to this fault model (Figure S6), and the aftershocks during just the first hour after the mainshock (Figure 7 in Obana et al., 2014) also align better with the fault for a strike of $\phi = 113°$. There is a possibility that multiple faults with different strike activated during the mainshock, but we have not

3

been able to resolve this complexity even with the multi-point-source inversion, due to overlapping interference.

Text S2. Finite-faulting investigation of the 2018 Nikol'skoye M_W 7.3 event.

The 2018 mainshock has a GCMT solution mechanism that is predominantly oblique-normal faulting with a large non-double component (Figure 1). The best double-couple faulting geometries have strike, $\phi_1 = 58°$, dip $\delta_1 = 68°$, rake $\lambda_1 = -19°$; and $\phi_2 = 155°$, $\delta_2 = 73°$, $\lambda_2 = -156°$, for a centroid depth of 17.6 km and centroid time shift of 8 s. The USGS-NEIC hypocenter depth is 16.6 km, and the USGS-NEIC W-phase solution, with $M_0 = 1.0 \times 10^{20}$ N-m (M_W 7.3), has a 43% double couple with best double-couple faulting geometries of $\phi_1 = 230°$, $\delta_1 = 70°$, $\lambda_1 = -40°$, and $\phi_2 = 336°$, $\delta_2 = 53°$, $\lambda_2 = -156°$ for a centroid depth of 19.5 km (https://earthquake.usgs.gov/earthquakes/eventpage/us2000ivfw/executive). The overall 60-day aftershock distribution has depths less than 23 km distributed over a swath 50 km by 100 km wide elongated in the northeast-southwest direction. There are several internal seismicity trends in a northwest-southeast direction, and the aftershock GCMT focal mechanisms (Figure 4d) have a diversity of strike-slip, oblique-normal and oblique compressional mechanisms that do not constrain a favored rupture plane, and cannot be reconciled with the sequence being confined to a single fault.

Similar to the 2010 Ogasawara event, the Nikol'skoye mainshock is at large distance from land, so we rely on seismic observations to characterize the rupture. Short-period back-projections of large regional network recordings of short-period (0.5-2 s) teleseismic P waves in North America, the southwest Pacific, and Europe/Greenland are performed (Figure S7). Locations of coherent short-period radiation found within 30 s of the rupture onset indicate a trend along the northeast direction from the source for the North America and European/Greenland networks. This is likely influenced somewhat by array response limitations. The IRIS back-projections for 0.25-1.0 Hz P wave data for North America are similar, but there is less of a northeastward trend in the images found from Europe and Australia networks (https://ds.iris.edu/spud/backprojection/17273627). These back-projections indicate rather concentrated source radiation and do not provide robust constraint on rupture velocity, but there is a mild preference for a northeast-southwest oriented fault plane rather than a northwest-southeast oriented fault plane.

We again perform finite-fault slip inversions of teleseismic broadband P and SH waveforms for both candidate fault planes for the GCMT and W-phase geometries noted above, along with many perturbations of those geometries, finding it difficult to confidently resolve the fault plane and slip distribution. A 1D velocity model from model Crust2 with a uniform water layer 4.5 deep is used for the source region structure. Our inversions for the USGS-NEIC W-phase best-double couple geometries consistently give similar (within a few percent) residual waveform power reduction for

4

either plane, with either choice failing to predict the first 10 s of the P waveforms at stations to the north and to the southeast. Similar misfits are noted for the USGS-NEIC finite fault solution (https://earthquake.usgs.gov/earthquakes/eventpage/us2000ivfw/finite-fault), which favors the northwest trending solution. However, the most distinctive difference in the waveform fits is found for *SH* waveforms, which are systematically better-fit for the northeast trending fault in our solutions. Figure S8 shows a slip inversion result for $\phi = 230°$, $\delta = 66°$, slightly modified in dip from the *W*-phase solution. This model is parameterized with 18 7.5-km-long subfaults along strike and five 5-km wide subfaults along dip, with the hypocenter at 11 km. 88 broadband *P* waves with excellent azimuthal distribution and 62 broadband *SH* waves are included in the inversion. A kinematic rupture expansion velocity of 4.0 km/s is used, with subfault source time functions parameterized with 23 1-s rise-time triangles offset by 1-s each, allowing up to 24 s subfault durations. The 4.0 km/s expansion velocity is not well constrained by the data, but by allowing the relatively long subfault source time function parameterization, we find very similar slip distributions for values from 2.0 to 4.5 km/s, so the overall slip model is relatively stable for a chosen fault orientation. For this southwest striking plane, the slip model has a primary slip patch extending from 5 to 13 km deep, with peak slip of ~6.0 m. This model has a slip-weighted average stress drop of 16 MPa (following the procedure in Ye et al., 2016), with individual subfault source time functions generally indicating multiple short duration slip pulses. The USGS-NEIC finite fault solution, for $\phi = 338°$, $\delta = 52°$, also finds slip of up to 5 m concentrated in the crust (https://earthquake.usgs.gov/earthquakes/eventpage/usp000hr97/finite-fault).
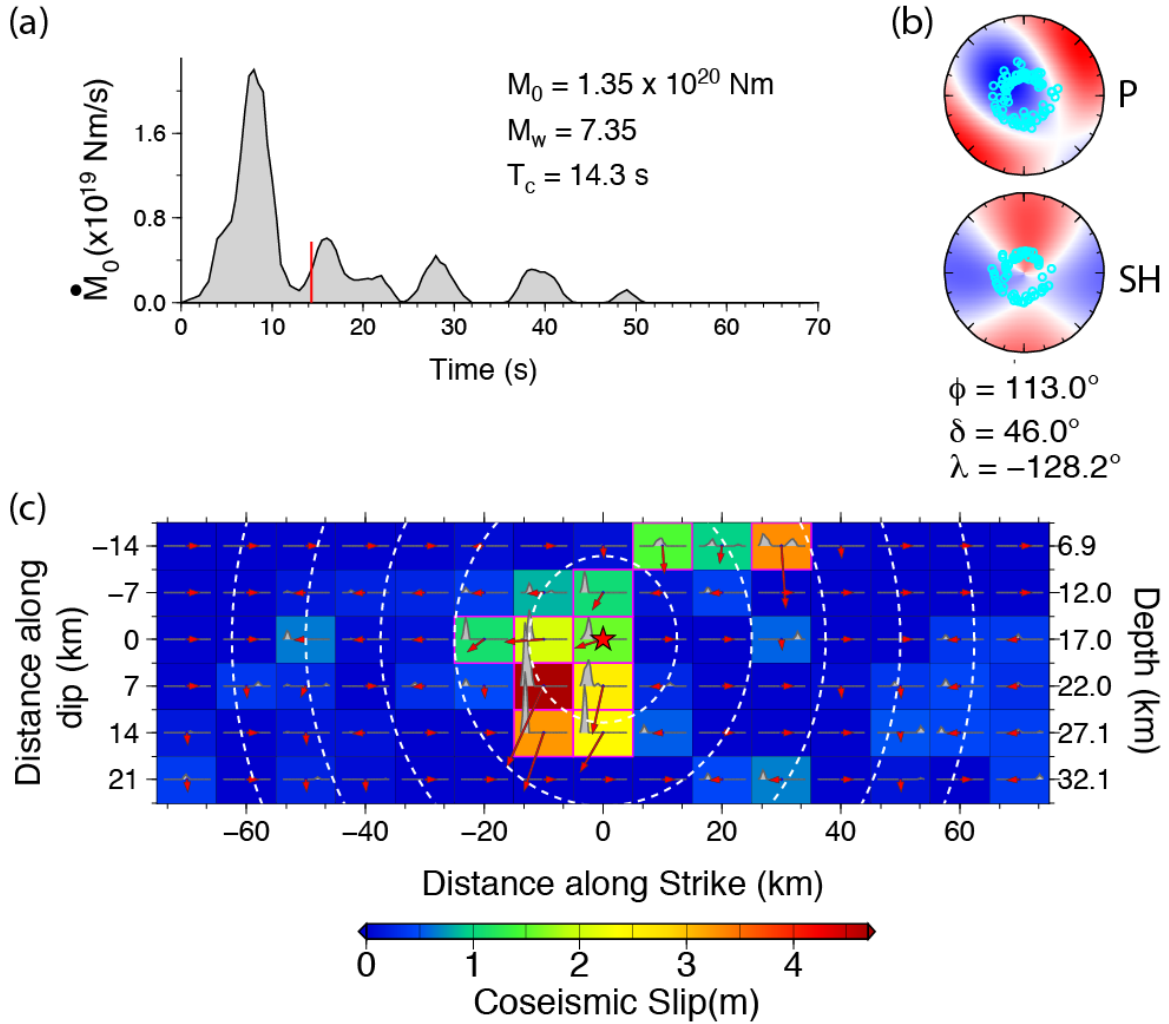
The moment-rate function (Figure S8a) is most reliable for the first 30 s, and has some short period jaggedness, as also seen in the USGS-NEIC solution. Comparison of the observations and predictions from this model (Figure S9) shows that the first ~35 s of the *P* and *SH* signals are well modeled at many azimuths, but there is poor fitting of the initial *P* wave onset at azimuths to the north and northeast and to the southeast. Perturbation of the planar model geometry did not resolve this. Application of the multiple-point source inversion to the first 30 s of the waveforms does not provide a compelling subevent mechanism-change model that fits the data much better. There is substantial *P* wave coda amplitude after 30 s, which is only partially accounted for by late source pulses and water multiples. The bathymetric variations with azimuth from the source are substantial, and similar to the 2010 Ogasawara event, it appears necessary to account for 3D bathymetry to reliably assess whether there is truly any later source radiation.

The same holds for the alternate choice of northwest-trending fault plane. Results for an inversion with $\phi = 336°$, $\delta = 53°$ are presented in Figures S10 and S11. This model is similar to the USGS-NEIC solution, and again shows shallow slip, concentrated in the crust. The initial *P* waves to the north and northeast are slightly better fit, but there is a noticeable difference in the fit to the *SH* waves as eastern azimuths, for which the predictions have a single pulse, whereas the data have a double hump. This feature is

much better matched for the southwest-striking model (Figure S9). The distribution of aftershocks is no better aligned with the northwest-striking model (Figure S12). While there is clearly some unresolved complexity in the radiation for the first 10 s of the event, the trend in the back-projections and the improved fit to the SH waveforms lead us to slightly favor the model in Figure S8, which is shown in map view in Figure 3.
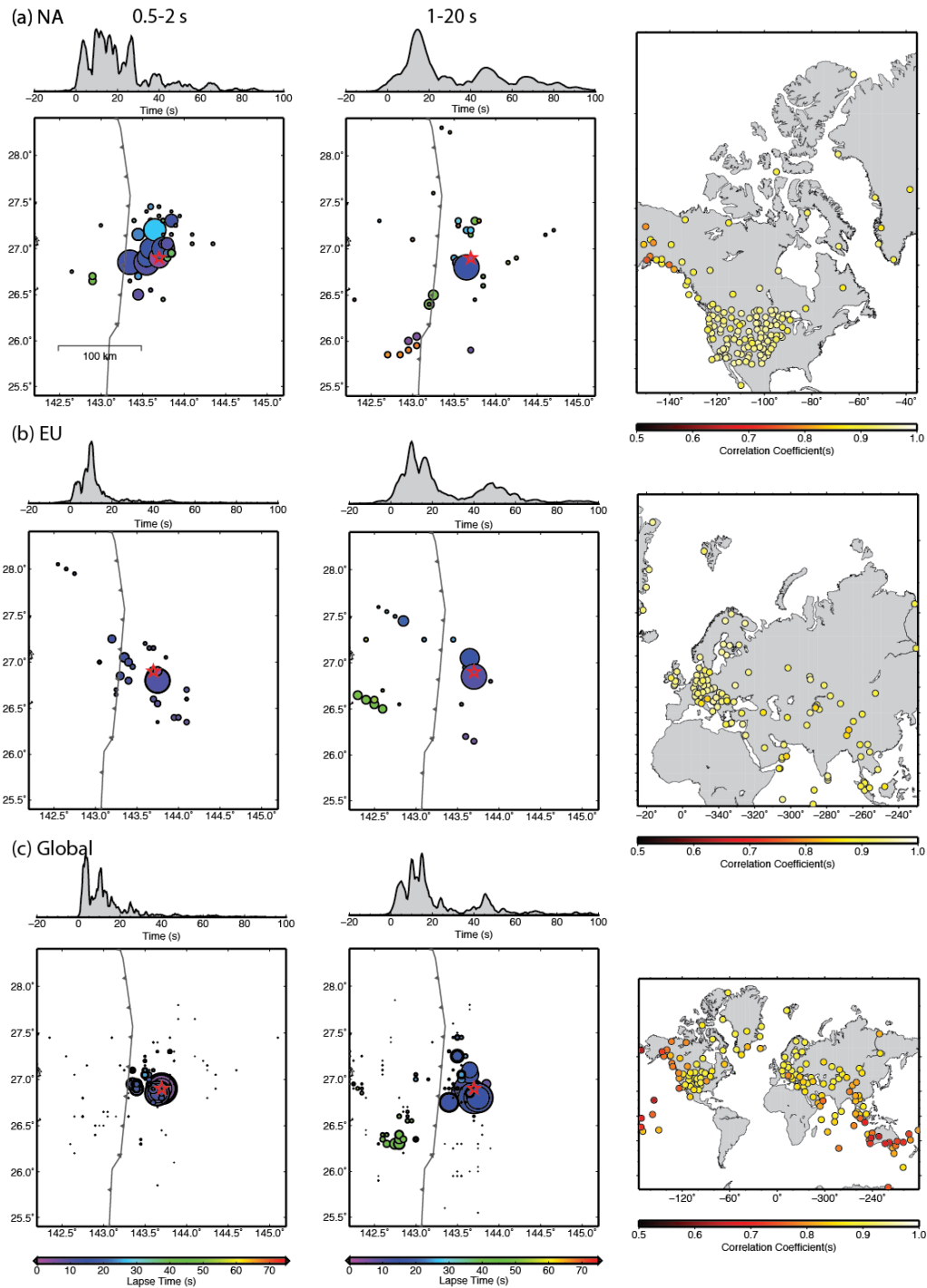
Figure S1. Summary of back-projections of short-period (0.5-2 s) and intermediate period (1-20 s) teleseismic *P* waves from the 2010 Ogasawara mainshock from regional networks in (a) North America (NA), (b) Eurasia (EU), and (c) a global network (Global). The loci of coherent short-period radiation are shown with circles proportional to power in the stack and color-coded by time in the left two columns, with the station distribution shown in maps on the right with symbols colored by the multi-channel correlation coefficient. Note the degredation in correlation for the global network.

Figure S2. Kinematic finite-fault inversion for the 2010 Ogasawara mainshock using broadband teleseismic *P* and *SH* waveforms. (a) The moment-rate function, with the total seismic moment (M_0), moment magnitude (M_W), and centroid time (T_c). The red tick mark indicates T_c on the time series. (b) Lower hemisphere, equal area *P* and *SH* focal mechanisms with the cyan circles indicating the distribution of paths to teleseismic observations used in the inversion. Blue regions in the *P* focal mechanism indicate dilational first-motions. (c) Slip distribution for the USGS-NEIC *W*-phase (Duputel) best-double-couple fault geometry with strike $\phi = 113°$, dip $\delta = 46°$, and a hypocenter depth 17 km. The subfault slip distribution is indicated by the color scale and by vectors indicating the slip direction of the hanging wall. Each subfault source time function, parameterized by 10 2-s rise time triangles lagged by 2 s, is shown as the gray polygon in each subfault. The initial rupture front velocity is specified as $V_r = 2.5$ km/s, with dashed white curves indicating the position in 5 s intervals. Observed and predicted waveforms are shown in Figure S3. The slip model is shown in map view in Figure 2. Solution for the alternate fault plane trending northwest is shown in Figures S4 to S6.
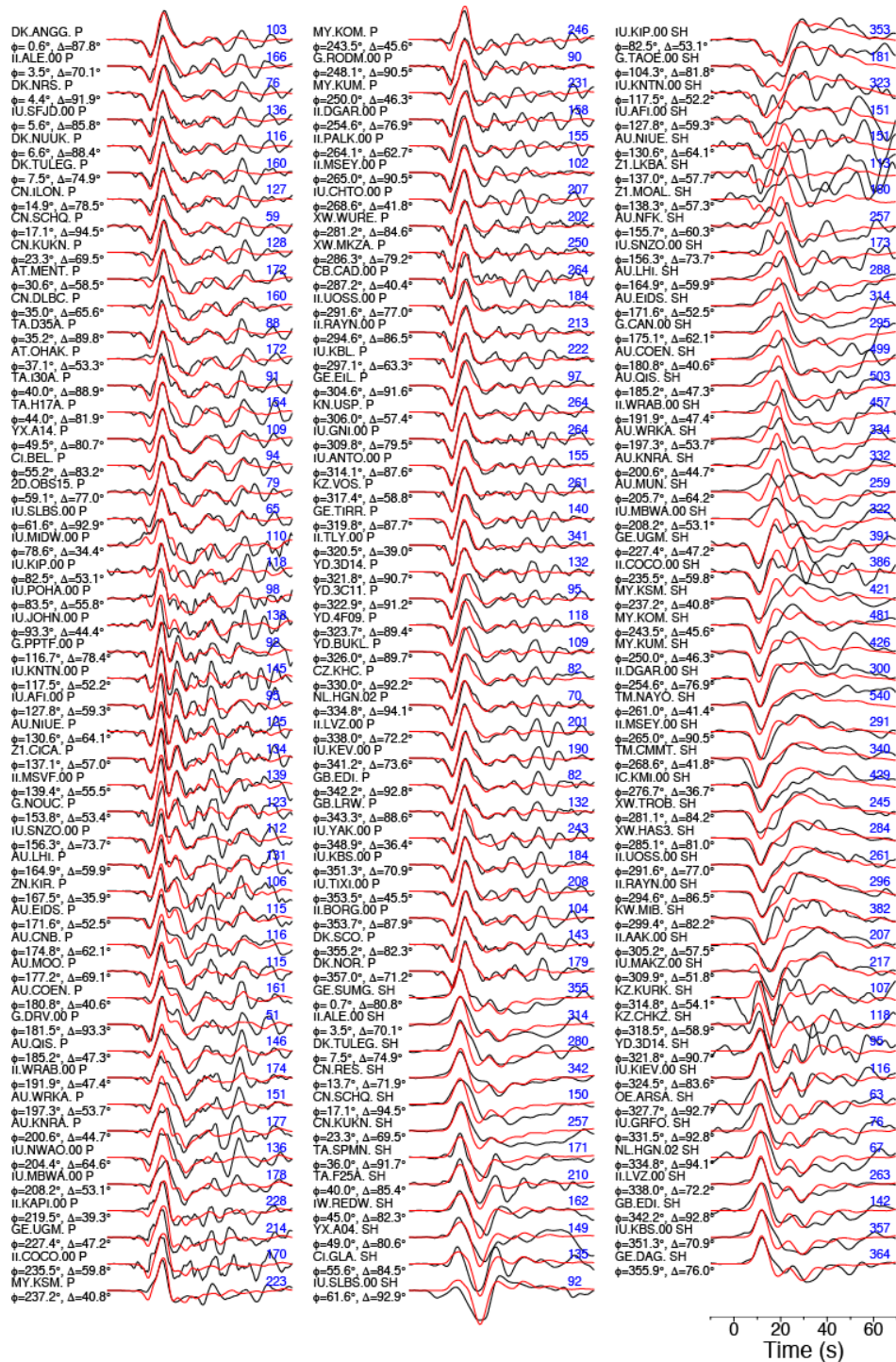
Figure S3. Comparison of observed (black) and computed (red) *P* and *SH* waveforms for the 2010 Ogasawara M_W 7.4 earthquake model shown in Figure S2. The traces in each comparison have correct relative amplitudes. The station name, phase, azimuth from the source (ϕ), and epicentral distance (Δ) is shown to the left of each trace pair, and the observed peak-to-peak amplitude (microns) of the observation is shown in blue on the right.

9
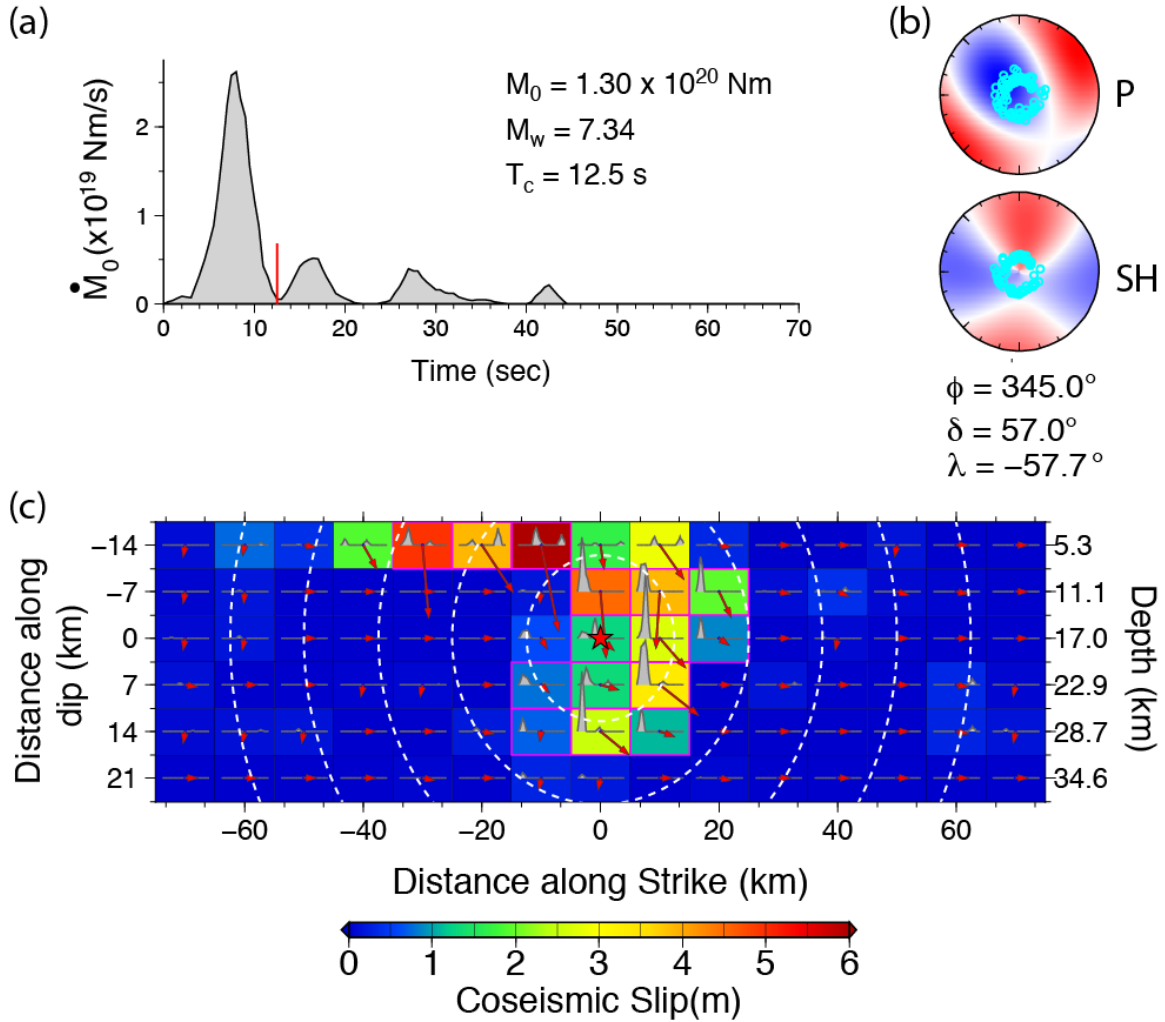
Figure S4. Kinematic finite-fault inversion for the 2010 Ogasawara mainshock using broadband teleseismic *P* and *SH* waveforms. (a) The moment-rate function, with the total seismic moment (M_0), moment magnitude (M_W), and centroid time (T_c). The red tick mark indicates T_c on the time series. (b) Lower hemisphere, equal area *P* and *SH* focal mechanisms with the cyan circles indicating the distribution of paths to teleseismic observations used in the inversion. Blue regions in the *P* focal mechanism indicate dilational first-motions. (c) Slip distribution for the USGS-NEIC *W*-phase (Duputel) best-double-couple fault geometry with strike $\phi = 345°$, dip $\delta = 57°$, and a hypocenter depth 17 km. The subfault slip distribution is indicated by the color scale and by vectors indicating the slip direction of the hanging wall. Each subfault source time function, parameterized by 10 2-s rise time triangles lagged by 2 s, is shown as the gray polygon in each subfault. The initial rupture front velocity is specified as V_r = 2.5 km/s, with dashed white curves indicating the position in 5 s intervals. Observed and predicted waveforms are shown in Figure S5.

10
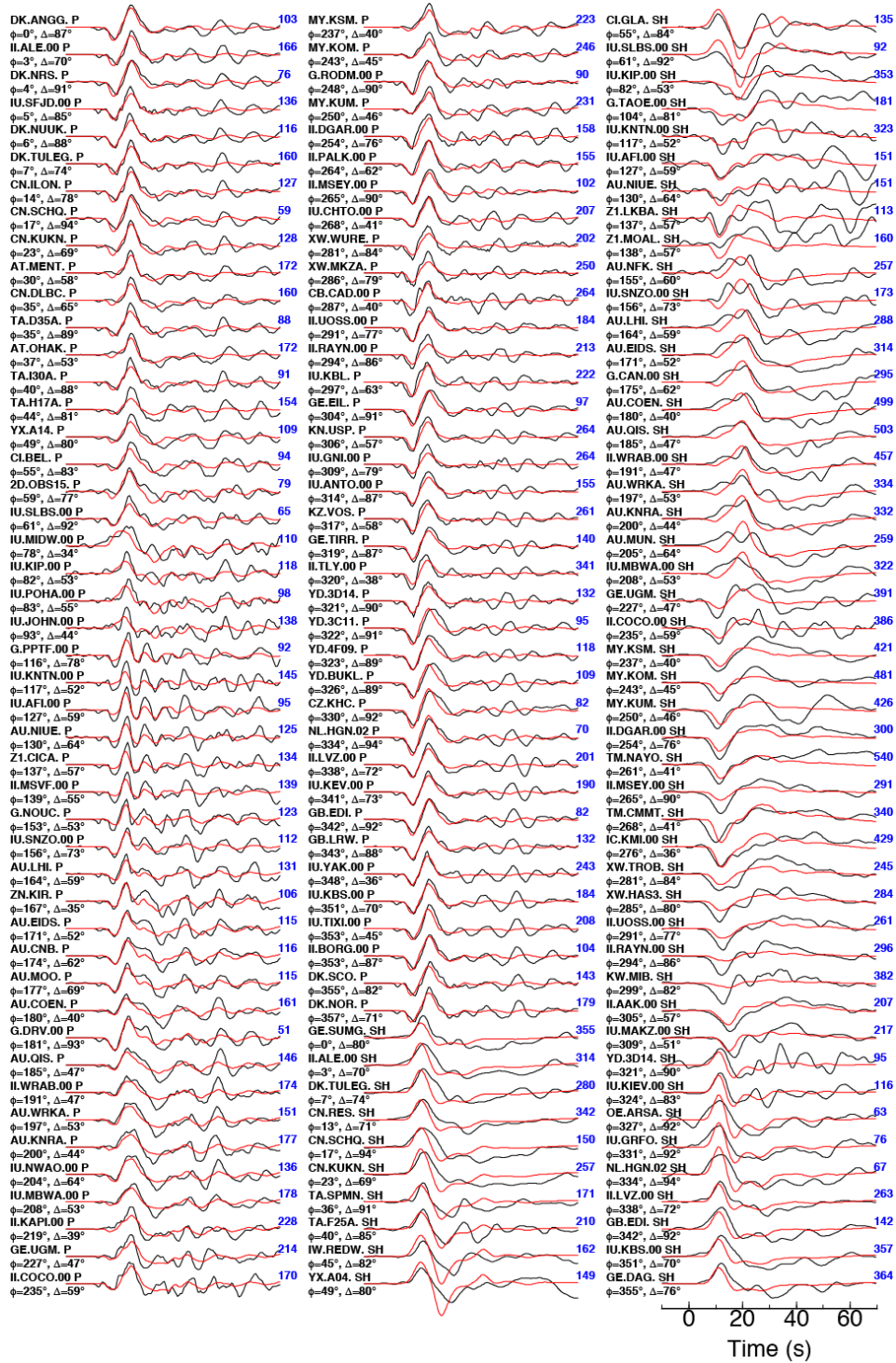
Figure S5. Comparison of observed (black) and computed (red) *P* and *SH* waveforms for the 2010 Ogasawara M_W 7.4 earthquake model shown in Figure S4. The traces in each comparison have correct relative amplitudes. The station name, phase, azimuth from the source (φ), and epicentral distance (Δ) is shown to the left of each trace pair, and the observed peak-to-peak amplitude (microns) of the observation is shown in blue on the right.

11
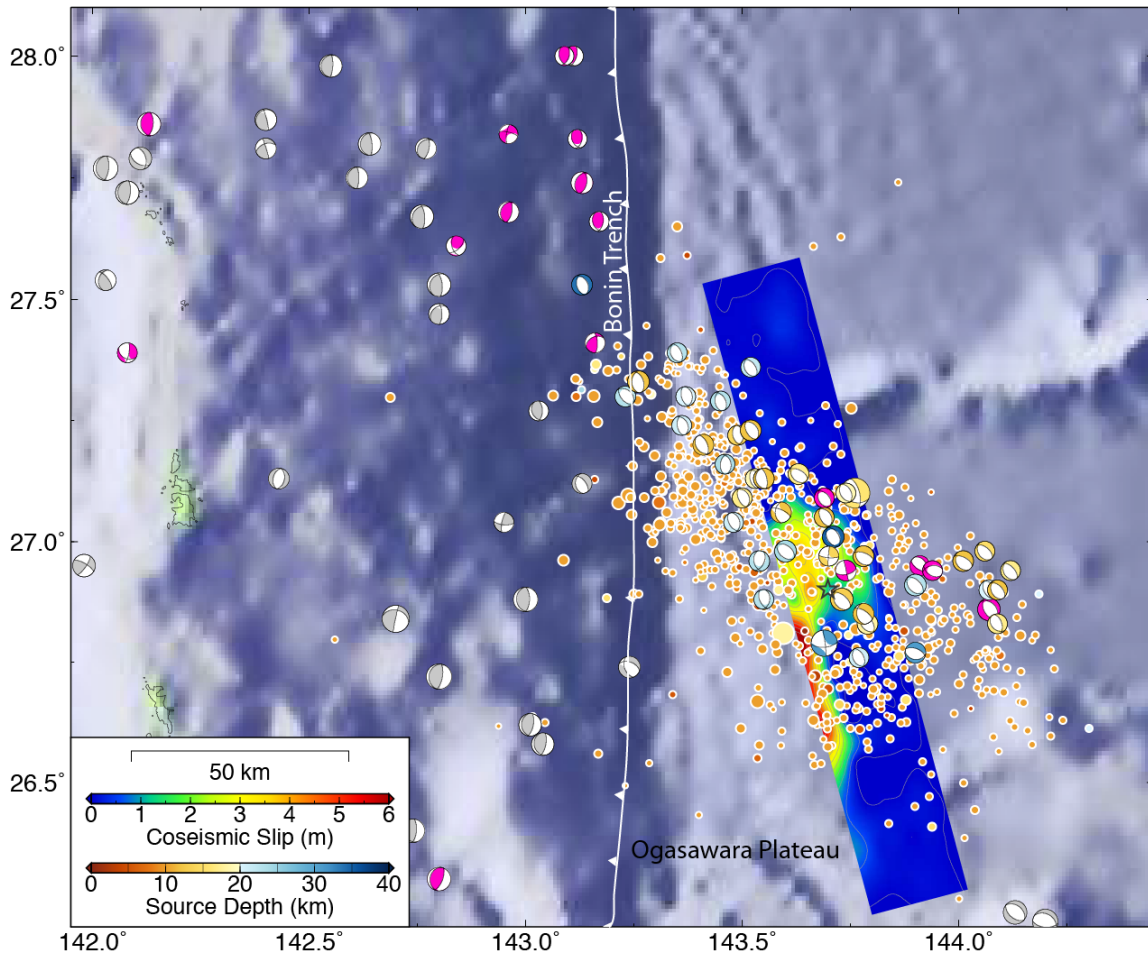
Figure S6. Map showing the 2010 Ogasawara M_W 7.4 mainshock finite-slip model from Figure S4 (the star indicates the mainshock epicenter) along with aftershocks in the first 60 days after the event from the USGS-NEIC catalog (circles colored by source depth and with radius proportional to magnitude), and from GCMT focal mechanisms plotted at the centroid locations, colored by centroid depth and scaled by M_W. Focal mechanisms colored in gray and magenta are for the time periods of 1976 to 2010 before the mainshock and 2011 to 2019 after the mainshock, respectively. The background bathymetry indicates the position of the Bonin trench trending north-south near longitude 143.2°, approximated by the white saw-toothed curve.
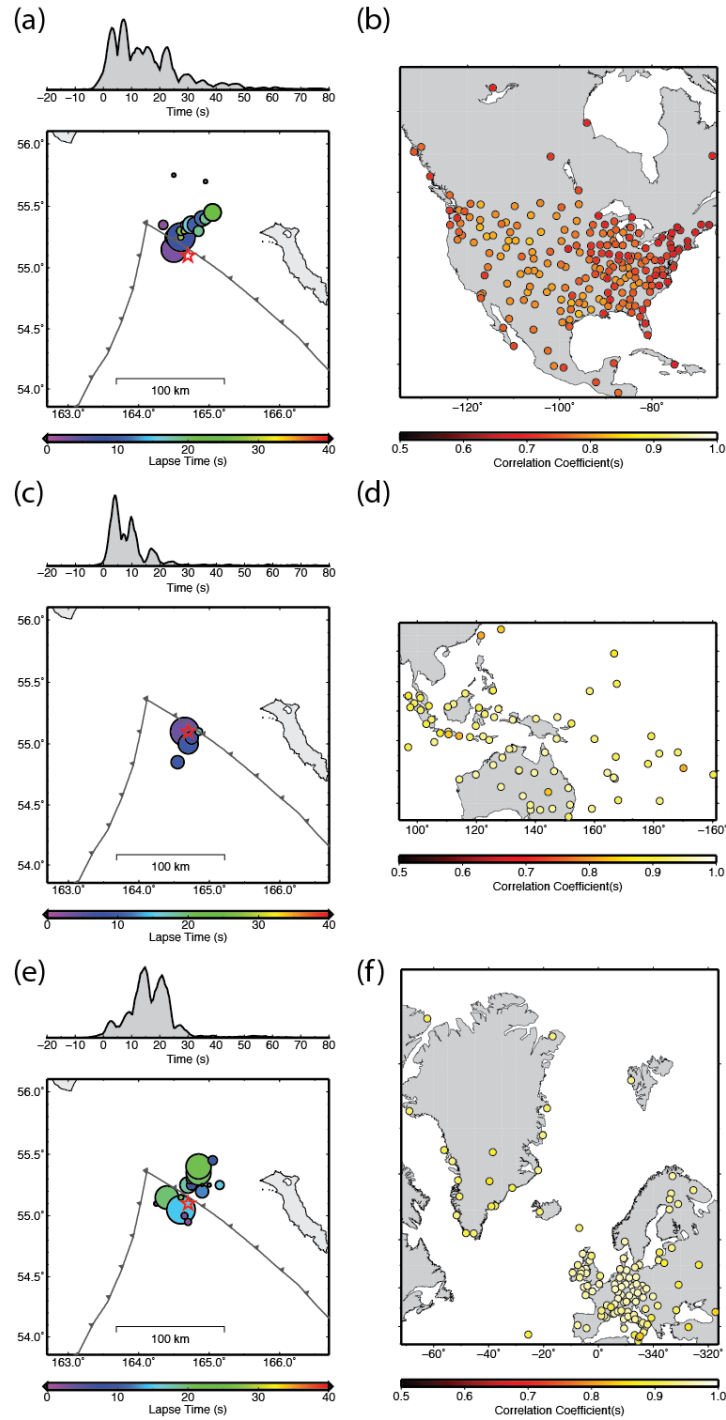
Figure S7. Summary of back-projections of short-period (0.5-2 s) teleseismic *P* waves from the 2018 Nikol'skoye mainshock from regional networks in (a) North America, (c) the southwest Pacific, and (e) Europe/Greenland. The loci of coherent short-period radiation are shown with circles proportional to power in the stack and color-coded by time. The respective station distributions are shown in (b), (d) and (f)), with symbols indicating the multi-channel correlation coefficient. Note the moderate correlations for North America, which is associated with near-nodal *P* waves.

13
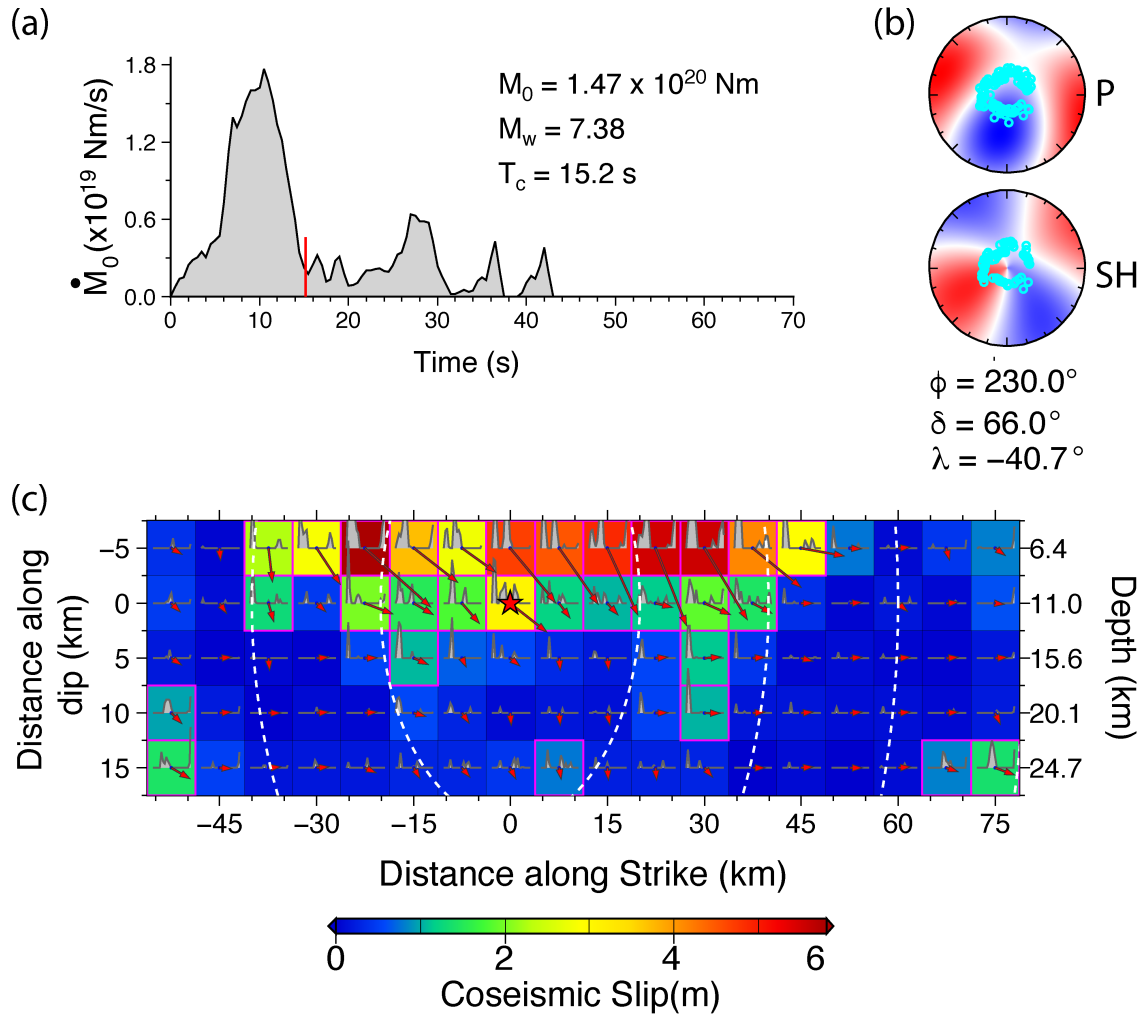
Figure S8. Kinematic finite-fault inversion for the 2018 Nikol'skoye mainshock using broadband teleseismic *P* and *SH* waveforms. (a) The moment-rate function, with the total seismic moment (M_0), moment magnitude (M_W), and centroid time (T_c). The red tick mark indicates T_c on the time series. (b) Lower hemisphere, equal area *P* and 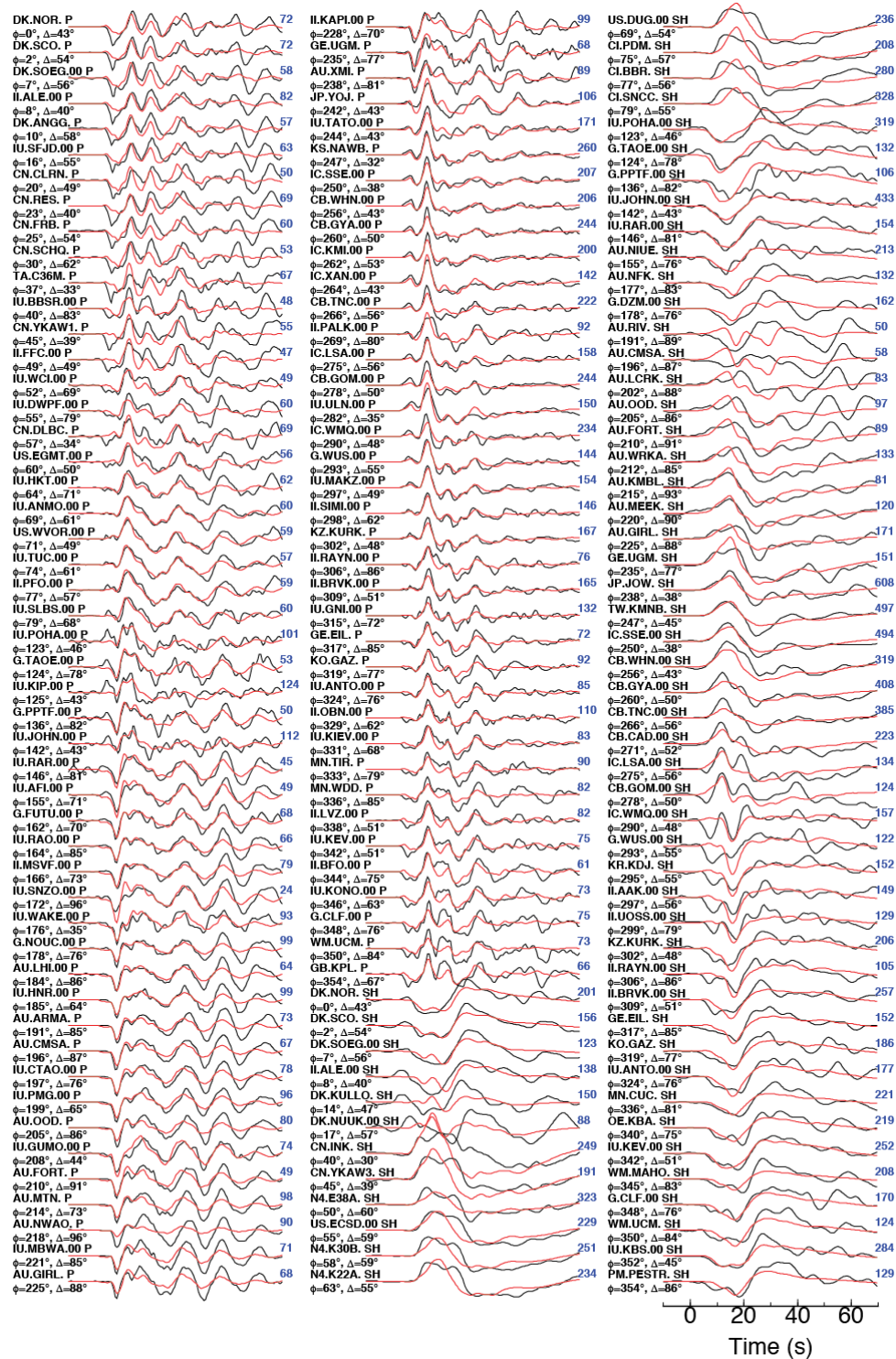*SH* focal mechanisms with the cyan circles indicating the distribution of paths to teleseismic observations used in the inversion. Blue regions in the *P* focal mechanism indicate dilational first-motions. (c) Slip distribution for the USGS-NEIC *W*-phase best-double-couple fault geometry with strike φ = 230°, dip δ = 66°, and hypocenter depth 11 km. The subfault slip distribution is indicated by the color scale and by vectors indicating the slip direction of the hanging wall. Each subfault source time function, parameterized by 23 1-s rise time triangles lagged by 1 s, is shown as the gray polygon in each subfault. The initial rupture front velocity is specified as V_r = 4.0 km/s, with dashed white curves indicating the position in 5 s intervals. Observed and predicted waveforms are shown in Figure S9. The slip model is shown in map view in Figure 3. Solution for the alternate fault plane trending northwest is shown in Figures S10 to S12.
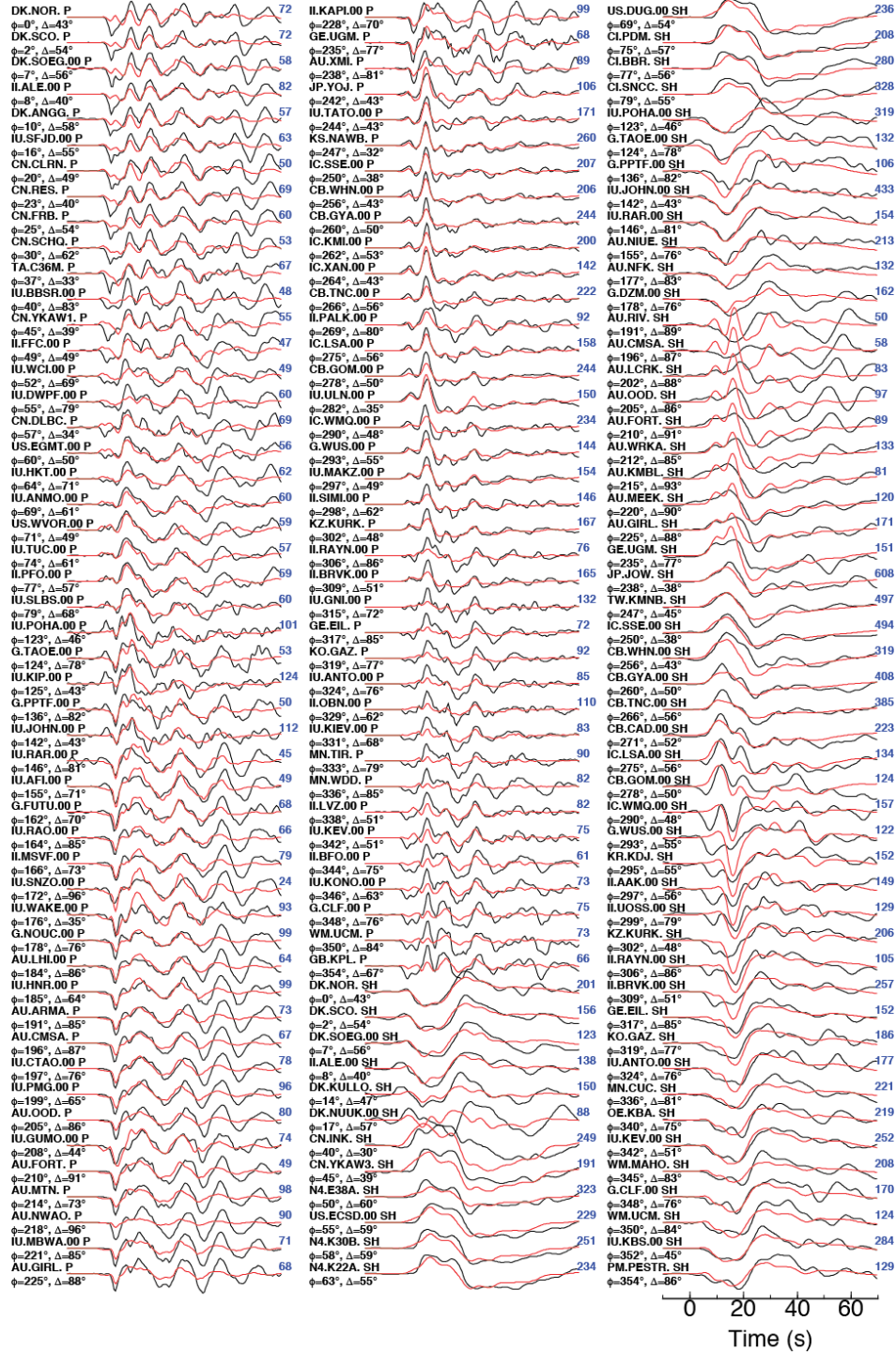
Figure S9. Comparison of observed (black) and computed (red) *P* and *SH* waveforms for the 2018 Nikol'skoye *M_W* 7.4 earthquake model shown in Figure S8. The traces in each comparison have correct relative amplitudes. The station name, phase, azimuth from the source (ϕ), and epicentral distance (Δ) is shown to the left of each trace pair, and the observed peak-to-peak amplitude (microns) of the observation is shown in blue on the right.

15

Figure S10. Kinematic finite-fault inversion for the 2018 Nikol'skoye mainshock using broadband teleseismic *P* and *SH* waveforms. (a) The moment-rate function, with the total seismic moment (M_0), moment magnitude (M_W), and centroid time (T_c). The red tick mark indicates T_c on the time series. (b) Lower hemisphere, equal area *P* and *SH* focal mechanisms with the cyan circles indicating the distribution of paths to teleseismic observations used in the inversion. Blue regions in the *P* focal mechanism indicate dilational first-motions. (c) Slip distribution for the USGS-NEIC W-phase best-double-couple fault geometry with strike $\phi = 336°$, dip $\delta = 53°$, and hypocenter depth 11 km. The subfault slip distribution is indicated by the color scale and by vectors indicating the slip direction of the hanging wall. Each subfault source time function, parameterized by 23 1-s rise time triangles lagged by 1 s, is shown as the gray polygon in each subfault. The initial rupture front velocity is specified as $V_r = 4.0$ km/s, with dashed white curves indicating the position in 5 s intervals. Observed and predicted waveforms are shown in Figure S11. Solution for the alternate fault plane trending southwest is shown in Figures 3, S8 and S9.

Figure S11. Comparison of observed (black) and computed (red) *P* and *SH* waveforms for the 2018 Nikol'skoye M_W 7.4 earthquake model shown in Figure S10. The traces in each comparison have correct relative amplitudes. The station name, phase, azimuth from the source (φ), and epicentral distance (Δ) is shown to the left of each trace pair, and the observed peak-to-peak amplitude (microns) of the observation is shown in blue on the right.

17
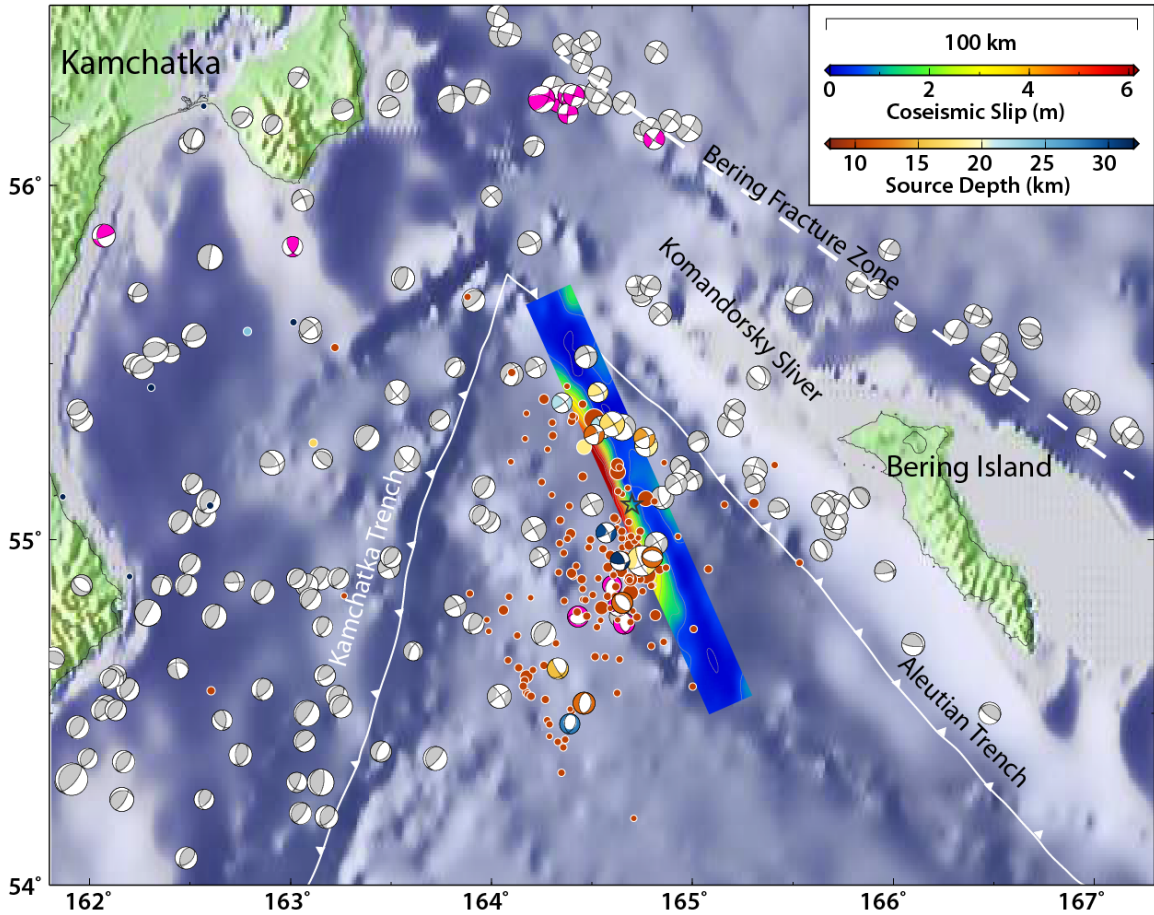
Figure S12. Map showing the 2018 Nikol'skloye M_W 7.4 mainshock finite-slip model from Figure S10 along with aftershocks in the first 60 days after the event from the USGS-NEIC catalog (orange circles with radius proportional to magnitude), and GCMT focal mechanisms plotted at the centroid locations, colored by centroid depth and scaled by M_W. Focal mechanisms colored in gray and magenta are for the time periods of 1976 to 2018 before the mainshock and 2018 to 2019 after the mainshock, respectively.